

CALIFORNIA STATE UNIVERSITY, NORTHRIDGE

Synthesis of Nitrogen-Doped Graphene  
on Copper from Azafullerene

A thesis submitted in partial fulfillment of the requirements  
For the degree of Master of Science in Physics

By

Joshua Neilson

August 2017

The thesis of Joshua Neilson is approved:

---

Dr. Simon Garrett

---

Date

---

Dr. Miroslav Peric

---

Date

---

Dr. Li Gao, Chair

---

Date

California State University, Northridge

## Acknowledgements

The research presented in this thesis would not have been possible without collaboration. I would like to thank Dr. Li Gao for his mentorship and patience throughout my graduate degree, Dr. Simon Garrett for his willingness to teach me about the XPS in great detail, and Prof. Liangbing Gan for his precursor molecule which has simplified and improved our research methods.

## Table of Contents

Signature Page .....	ii
Acknowledgements.....	iii
List of Figures .....	v
List of Tables .....	vi
Abstract.....	vii
1 Introduction.....	1
1.1 Motivation.....	1
1.2 Graphene Versus Doped Graphene.....	2
1.3 Methods of Preparing Doped Graphene.....	3
1.4 Reasons for Developing New Approach.....	4
1.5 Outline.....	4
2 Experimental Methods.....	5
2.1 Scanning Tunneling Microscopy.....	5
2.1.1 Principles.....	5
2.1.2 Theory.....	5
2.1.3 Unisoku STM.....	8
2.1.4 STM Tips.....	11
2.1.5 Molecular Evaporator.....	13
2.1.6 Data Acquisition.....	14
2.1.7 Spectroscopy.....	15
2.2 X-ray Photoelectron Spectroscopy.....	16
2.2.1 Principles.....	16
2.2.2 Theory.....	17
2.2.3 Physical Electronics XPS.....	20
2.2.4 Data Acquisition.....	21
2.2.5 Sample Transportation.....	21
3 Nitrogen-Doped Graphene on Cu(111).....	22
3.1 Sample and Precursor.....	22
3.2 Preparation.....	23
3.3 Synthesis.....	23
3.4 STM Results.....	27
3.5 STS Data.....	30
3.6 XPS Data.....	33
3.7 Discussion.....	34
4 Summary and Outlook.....	35
4.1 Summary.....	35
4.2 Potential Applications.....	35
4.3 Questions for the Future.....	35
Supplemental Information.....	36
S.1 Calculating Graphene Coverages.....	36
S.2 Plotting Line Spectroscopy Data with Igor Pro.....	37
References.....	39

## List of Figures

Figure 1 The A and B sublattices of graphene.....	1
Figure 2 Sketches of the energy-momentum dispersion relation $E(\mathbf{k})$ for intrinsic, $n$ -doped, and $p$ -doped graphene .....	3
Figure 3 Direction of electron tunneling due to sample and tip energies .....	6
Figure 4 Quantum tunneling of electrons between the sample and the tip across a vacuum barrier of width $s$ upon the application of a bias voltage $V$ .....	7
Figure 5 Bias-dependent STM images of N-doped graphene on Ru(0001) .....	8
Figure 6 Unisoku UHV low-temperature STM (USM 1500S) system and controllers.....	8
Figure 7 Schematic of the refrigerator and STM chamber .....	9
Figure 8 Schematic of the DC etching method for tip preparation.....	12
Figure 9 W tips prepared by DC etching and AC etching .....	12
Figure 10 Molecular evaporator by itself and installed to the P chamber .....	14
Figure 11 Crucible temperature versus filament current for the molecular evaporator....	14
Figure 12 Data acquisition using Nanonis software .....	15
Figure 13 Examples of point spectra and line spectra recorded on TiO <sub>2</sub> (001).....	16
Figure 14 Schematic of the photoemission process in XPS .....	17
Figure 15 Design of the hemispherical energy analyzer.....	19
Figure 16 Example of an XPS spectrum for N .....	19
Figure 17 XPS system and its controller.....	20
Figure 18 Data acquisition for the XPS .....	21
Figure 19 The Cu(111) sample in the preparation chamber .....	22
Figure 20 Synthetic chemistry of the C <sub>59</sub> NH molecule .....	22
Figure 21 STM image of clean Cu(111) surface .....	23
Figure 22 STM images before and after annealing the C <sub>59</sub> NH/Cu(111) sample.....	24
Figure 23 Atomic-resolution STM images of graphene with N dopants.....	25
Figure 24 N-doping configurations in graphene and Graphitic N on A and B atom.....	26
Figure 25 STM images of 0.14 ML N-doped graphene on Cu(111) .....	26
Figure 26 STM images of 0.35 ML N-doped graphene on Cu(111) .....	27
Figure 27 STM images of 1.0 ML N-doped graphene on Cu(111) .....	27
Figure 28 Two examples of dopant alignment along graphene edges.....	28
Figure 29 STM images showing the rings of N dopants on different graphene islands...	29
Figure 30 STS of N-doped graphene on Cu(111).....	31
Figure 31 dI/dV point spectra of N dopant and surrounding C atoms.....	32
Figure 32 dI/dV line spectra across the N dopant.....	32
Figure 33 XPS survey scan.....	33
Figure 34 XPS spectra of N 1s and C 1s.....	33

## List of Tables

Table 1 Some applications of heteroatom-doped graphene .....	2
Table 2 Tip etching solutions and conditions .....	11
Table 3 XPS anode materials .....	18

## Abstract

### Synthesis of Nitrogen-Doped Graphene on Copper from Azafullerene

By Joshua Neilson

Master of Science in Physics

Graphene is a fascinating material with many potential applications. Doping graphene with heteroelements like nitrogen is an effective approach to improving its performance in supercapacitors, transistors, batteries, fuel cells, solar cells, sensors, and gas storage. It is always desired to develop new approaches for the synthesis of large-scale, high-quality N-doped graphene with controlled doping properties. In this research, we have achieved the synthesis of N-doped single-layer graphene on the Cu(111) surface using the N-containing sole precursor azafullerene ( $C_{59}NH$ ). The synthesis process includes cycles of precursor deposition at room temperature and subsequent annealing in ultrahigh vacuum (UHV). The synthesis process and doping properties have been investigated on the atomic scale using scanning tunneling microscopy (STM) and X-ray photoelectron spectroscopy (XPS) measurements. The existence of graphitic and pyridinic N atoms in the graphene layer is suggested by STM and XPS results. For the first time, we observed the rings of N dopants, which provide valuable information about the growth process.

# 1 Introduction

## 1.1 Motivation

Graphene is an incredibly interesting substance with a variety of applications. Predicted to exist as early as 1947, graphene is a single atomic layer of C atoms arranged in a perfect hexagonal honeycomb lattice.<sup>1,2</sup> The neighboring sites of the lattice are not equivalent due to the directionality of the bonds formed between each atom. Thus, graphene is composed of two sublattices (A and B) as pictured in Figure 1.<sup>3</sup> Graphene is impermeable to gases, stronger than steel, a better electrical conductor than silver, and more thermally conductive than copper.<sup>1,4</sup> Graphene is also transparent, absorbing only 2.3% of incident white light per layer.<sup>5</sup> These properties have inspired scientists and engineers alike to investigate graphene's possible applications in electronics, coatings, semiconductors, medical devices, DNA sequencing, batteries, fuel storage, photovoltaics, and much more.<sup>1,6,7</sup> It is the first discovered two-dimensional crystal in existence, and its unique characteristics have earned it the moniker of “wonder material”.<sup>1</sup>

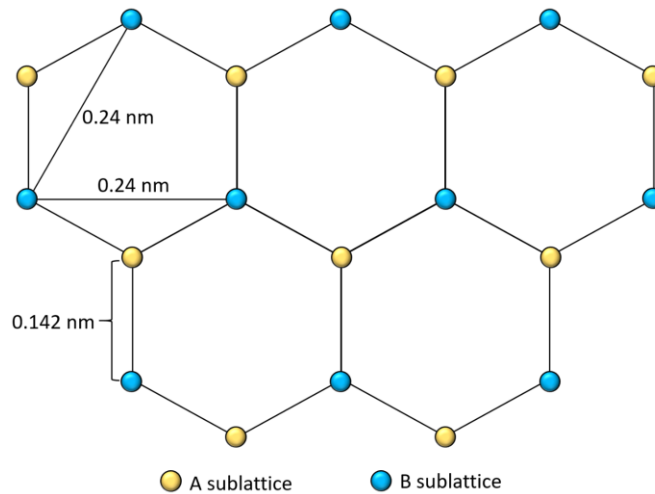


Figure 1 The A and B sublattices of graphene<sup>3</sup>

The isolation of graphene was first achieved in 2004 by the Geim research group at The University of Manchester.<sup>8</sup> The isolation was performed mechanically by repeatedly peeling off graphite layers with Scotch tape. This method was surprisingly more efficient than using expensive polishing equipment. The group proceeded to investigate the electrical properties of the atomically thin carbon films.<sup>9</sup> Due to their success in producing, isolating, identifying, and characterizing graphene, Andre Geim and Konstantin Novoselov were awarded the Nobel Prize in Physics in 2010.<sup>1</sup>

The techniques used to synthesize graphene have become more advanced in the thirteen years since its initial isolation. Graphene can be obtained using mechanical exfoliation, burning SiC surfaces, atomic force microscope manipulation of graphite crystals, chemical vapor deposition, and other methods.<sup>1</sup> Methods for synthesizing graphene on large scales continue to improve as graphene research advances across the world.<sup>10</sup>

In addition to developing graphene on large scales, it is also a key area of interest to manipulate the graphene lattice and tailor its properties. This can be done in a variety of ways. The main motivation for our research is to develop a method for tuning these properties by controlled doping of graphene with N.

## 1.2 Graphene Versus Doped Graphene

“Doped” graphene is when elements other than C (usually N or B) are substituted into the otherwise pure graphene lattice. Properties of the graphene change in this case, even with small amounts of dopants. These small changes can have large implications with a range of practical applications.

*Table 1 Some applications of heteroatom-doped graphene*<sup>6,11</sup>

<b>Applications</b>	<b>Advantages of doping effects</b>
Supercapacitors	Enhanced electrochemical activity; lower charge-transfer resistance; better sheet-to-sheet separation; improved conductivity than graphene oxide precursors
Lithium ion batteries	Achieving balance between Li binding and diffusion; enable abundant and uniform loading of metal oxide nanoparticles
Fuel cells	Induced charge polarization and spin density enhances oxygen adsorption and cleavage; enable abundant and uniform loading of metal nanoparticles
Solar cells	Increases the catalytic activity of dye sensitized solar cells counter electrode; endows graphene with p or n doping effect; increase graphene work function
Sensors	Facilitates charge transfer, analyte adsorption and activation; assists anchoring of functional moieties or molecules; opens graphene bandgap, induces charge polarization
Gas storage	Increases binding affinity towards gas molecules, especially CO <sub>2</sub> , compared to other state-of-the-art techniques; enables abundant and uniform loading of metal nanoparticles

Graphene can be doped in two ways, *n*-doping and *p*-doping. With *n*-doping, negatively (*n*) charged electrons are added to the graphene. Conversely, *p*-doping removes electrons from graphene. The influence of doping on the electronic structure of graphene is sketched in Figure 2, which shows the energy-momentum dispersion relation  $E(\mathbf{k})$  for intrinsic

graphene, *n*-doped graphene, and *p*-doped graphene according to  $p = \hbar k$ , where  $p$  is the momentum,  $\hbar$  is Planck's constant  $h/2\pi$ , and  $k$  is the wave number equal to  $E/\hbar c$ .

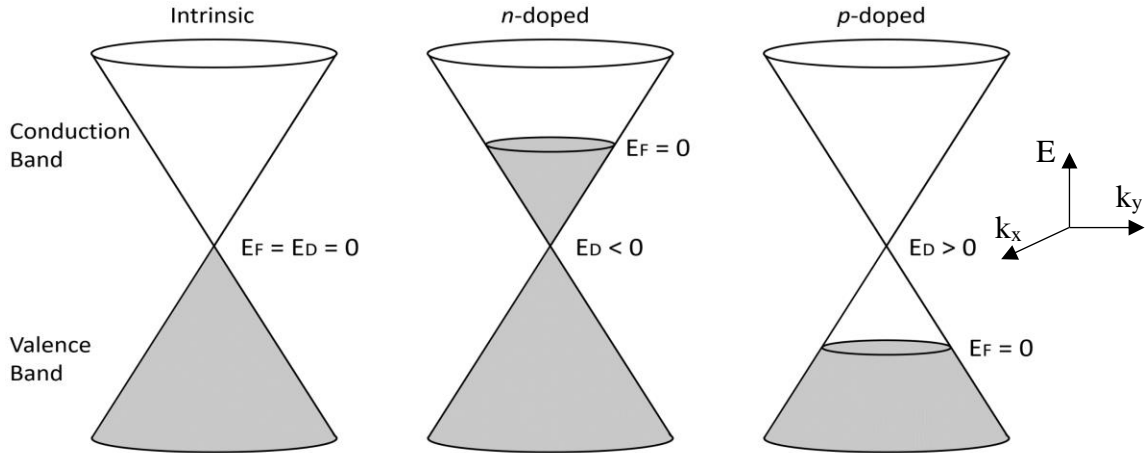


Figure 2 Sketches of the energy-momentum dispersion relation  $E(\mathbf{k})$  for intrinsic, *n*-doped, and *p*-doped graphene

The gray regions in Figure 2 represent occupied energy levels of the graphene. The Fermi energy  $E_F$  is the energy difference between the highest and lowest occupied energy states, and the Fermi level corresponds to zero voltage bias in  $dI/dV$  measurements. For intrinsic graphene,  $E_F$  is at the Dirac point where the valence band and conduction band meet. The Dirac point  $E_D$  shifts downward relative to  $E_F$  for *n*-doping, and shifts upward relative to  $E_F$  for *p*-doping. In this work, we focus on N dopants. Previous studies indicate that graphitic N leads to *n*-doping and pyridinic N leads to *p*-doping.<sup>6</sup>

### 1.3 Methods of Preparing Doped Graphene

There are many methods used for preparing doped graphene including chemical vapor deposition, ball milling, bottom-up synthesis, thermal annealing, the wet chemical method, plasma, photo-chemistry, and arc-discharge.<sup>6</sup> Previous studies have shown that graphene can be synthesized using a Buckminsterfullerene  $C_{60}$  precursor molecule.<sup>12</sup> The  $C_{60}$  molecule can be modified by substituting one or several C atoms with other atoms. Recently, we have achieved the controlled synthesis of N-doped graphene on Ru(0001) by using the sole precursor  $C_{59}NH$  (known as azafullerene). In this work, we study the synthesis of N-doped graphene on the Cu surface by using the sole precursor  $C_{59}NH$ . The  $C_{59}NH$  molecules were synthesized by Prof. Liangbing Gan's lab at Peking University in China.

#### 1.4 Reasons for Developing New Approach

Heteroatom-doped graphene is commonly prepared using multiple precursor molecules (for example,  $\text{CH}_4$  and  $\text{NH}_3$ ),<sup>6</sup> but there are a few main advantages to using a sole precursor molecule. First, it will greatly increase the simplicity of cultivating large-scale doped graphene for both scientific and industrial purposes. Second, choosing different precursors, substrates, and synthesis parameters will allow us to control the doping properties. Third, high doping homogeneity can potentially be attained since the composite elements are both from the same precursor.<sup>13</sup> So far, the studies of the synthesis of doped graphene using sole precursors are limited.<sup>10,14</sup> One potentially convenient approach for controlling the N-doping concentration is to choose sole precursors with different N contents.

In this work, we study how the distribution of dopants changes with increasing cycles of deposition and annealing of the sole precursor molecule  $\text{C}_{59}\text{NH}$  on the Cu(111) surface. Cu was selected as our substrate due to the fact that graphene on Cu can be easily transferred onto other substrates for practical applications. There are several methods used to accomplish this. A common technique involves dissolving the Cu substrate away using an aqueous solution of iron nitrate. The new substrate can then be brought into contact with the free graphene film in the solution. Alternatively, the graphene can be coated with polydimethylsiloxane (PDMS) or poly-methyl methacrylate (PMMA) prior to etching. This coating step tends to result in a more durable graphene film.<sup>15</sup>

#### 1.5 Outline

Chapter 2 of this thesis will discuss the experimental methods used in this research. Specifically, it will elaborate on the history, principles, and theory of scanning tunneling microscopy (STM) and X-ray photoelectron spectroscopy (XPS) along with specific technical information about each technique. Chapter 3 will detail our experiment with N-doped graphene on Cu(111) including preparation methods, experimental techniques, results, and discussions. Chapter 4 will provide a summary of this thesis and outline possible applications of our results as well as questions and ideas for future experiments.

## 2 Experimental Methods

### 2.1 Scanning Tunneling Microscopy

In 1981, Gerd Binnig and Heinrich Rohrer developed the first scanning tunneling microscope based on the concept of quantum tunneling.<sup>16</sup> Their work earned them the Nobel Prize in Physics in 1986.<sup>17</sup> The first STMs were much simpler than they are today, though the images they produced were revolutionary in their detail. These were the first images of surfaces at the atomic scale, and even the simplest ones provided incredible new insights on structural microscopy, local displacement monitoring, and spectroscopy.<sup>16</sup>

#### 2.1.1 Principles

Scanning tunneling microscopy is completed by passing a sharp conducting tip over, and very close to, a sample of interest. A bias voltage is applied to the sample causing a current to flow between the sample and tip. Feedback loops control piezos attached to the tip to maintain a constant tip height or tunneling current as the tip moves across the surface. The tip height and tunneling current are recorded using data acquisition software to form a topographical image of the sample surface.

#### 2.1.2 Theory

The scanning tip never actually touches the substrate surface. The STM relies on quantum tunneling to be able to produce images. Quantum tunneling is when a particle, like an electron, travels through a potential barrier. This type of motion would be forbidden in classical mechanics, but physics at the quantum scale exploits the evanescent wave properties of surface electrons in order to permit the tunneling effect.<sup>18</sup> In the case of the STM, the potential barrier is the ultra-high vacuum which separates the scanning tip from the sample surface. With a bias voltage applied between the tip and sample, a number of electrons are able to tunnel through the vacuum barrier resulting in a current. The direction of electron tunneling depends on the polarity of the bias voltage. Positive biases result in electron tunneling from occupied states in the tip to unoccupied states in the sample, and negative biases result in the opposite as illustrated in Figure 3. In principle, other barriers (air, water, etc.) may also be used, though vacuum is preferable due to a decreased risk of surface contamination and tip wear.<sup>19</sup>

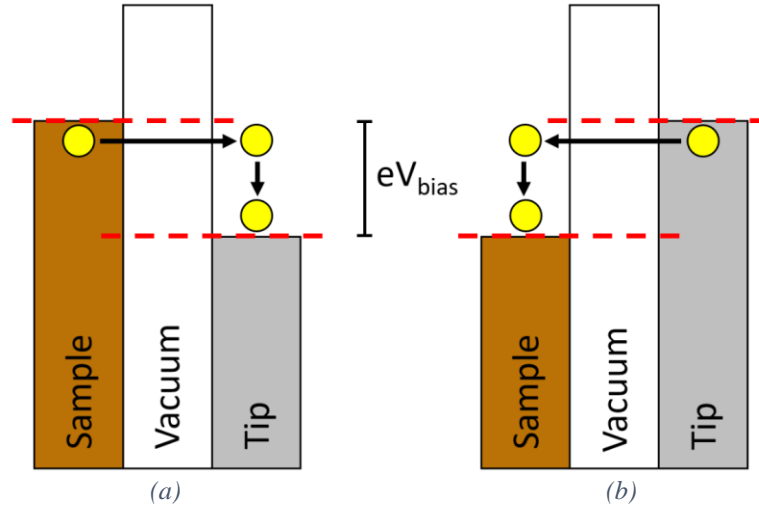


Figure 3 Direction of electron tunneling due to sample and tip energies  
 (a) Sample at negative bias (b) Sample at positive bias

As the tip moves across the sample lattice, the probability of an electron tunneling varies with position. When scanning in constant-height mode, the dark regions in the image produced by the STM represent regions where fewer electrons were able to tunnel given a constant separation between the tip and sample. In constant-current mode, the dark regions correspond to areas where the tip had to get closer to the surface to maintain the same set-point current.

A precise mathematical formulation of this behavior is impossible without specific knowledge of the tip states. In general, quantum tunneling can be described mathematically by solving the Schrödinger equation for an electron in a classically forbidden region ( $E < U$ ):

$$-\frac{\hbar^2}{2m} \frac{d^2}{dz^2} \Psi(z) + U(z)\Psi(z) = E\Psi(z)$$

where  $\hbar$  is Planck's constant  $h/2\pi$ ,  $m$  is the mass of the electron,  $z$  is the distance the electron travels through the barrier,  $\Psi$  is the wave function,  $U$  is the potential energy of the electron, and  $E$  is the total energy of the electron. The solutions are given by:

$$\Psi(z) = \Psi(0)e^{-kz}$$

where  $k = \frac{\sqrt{2m(U-E)}}{\hbar}$  is the decay constant. Since the probability of tunneling decreases exponentially with increased distances, small changes in the separation between the tip and sample can correspond to relatively large changes in the tunneling current.<sup>20</sup> The tip-sample separation distance is usually only a few Å during scanning.

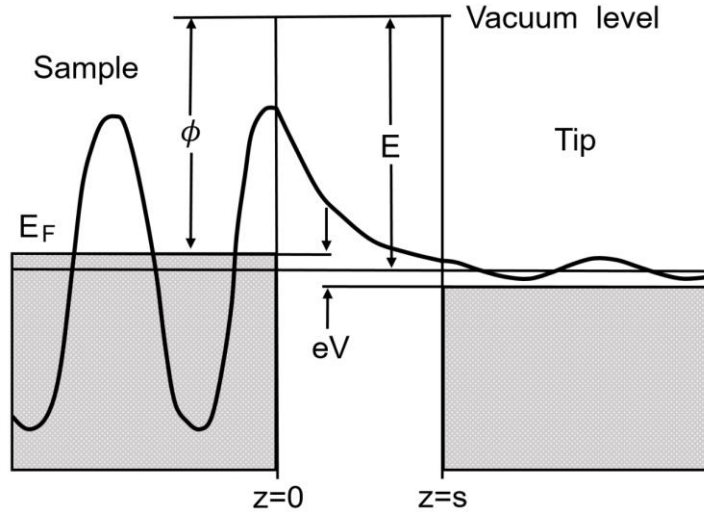
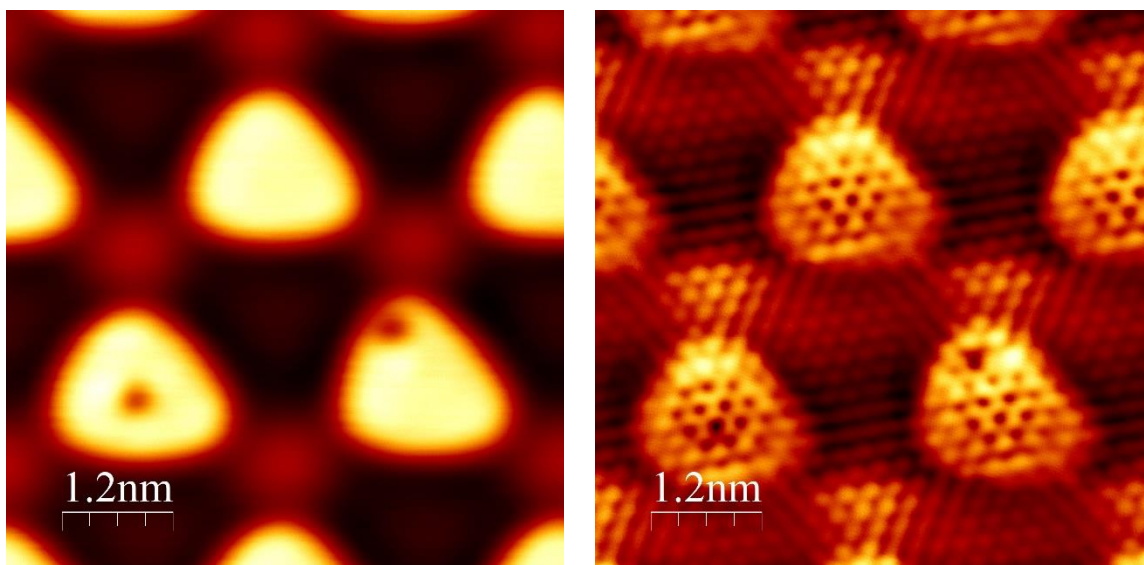


Figure 4 Quantum tunneling of electrons between the sample and the tip across a vacuum barrier of width  $s$  upon the application of a bias voltage  $V$ <sup>20</sup>

Figure 4 shows the wave behavior of a tunneling electron. The tip and sample are separated by a distance  $s$ . The figure also reinforces the important concept of the Fermi level  $E_F$  (the limit of a metal's occupied states) and introduces the work function  $\Phi$  (the minimum energy needed to move an electron from the metal into vacuum).<sup>20</sup> The relevant work functions for our experiment are 4.6 eV for Cu and 4.8 eV for W.<sup>21</sup> An important detail in tunneling is that while the probability amplitude shrinks after passing through the barrier, tunneling has no effect on the frequency.

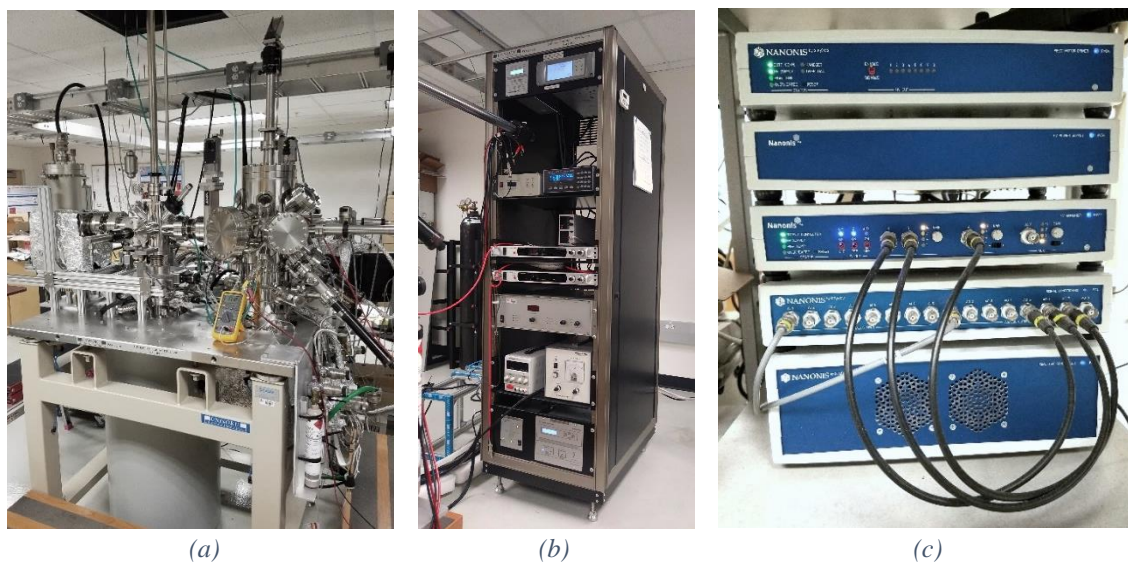
Changing the bias voltage of the sample can cause tunneling to occur from different electron energy levels. In Figure 5 below, the same area on the N-graphene/Ru(0001) surface was scanned with two different bias voltages. Although both images prominently show the Moiré pattern, the image in (b) exhibits atomic-resolution while the image in (a) does not. The STM images are also dependent on the tip status.



(a) (b)  
 Figure 5 Bias-dependent STM images of N-doped graphene on Ru(0001)<sup>13</sup>  
 (a) Size: 6 nm × 6 nm; Scanning Parameters: 1 V, 50 pA  
 (b) Size: 6 nm × 6 nm; Scanning Parameters: 10 mV, 1 nA

### 2.1.3 Unisoku STM

A Unisoku ultra-high vacuum (UHV) low temperature STM (USM 1500S) system was used for this research. It was installed in 2013 and modified to fit the needs of the lab. The entire apparatus rests on a floating table that acts as a passive noise filter. An adjacent controller unit (Figure 6(b)) monitors chamber pressures and temperatures and houses equipment used for pumping, sputtering, annealing, tip processing, and molecular deposition.



(a) (b) (c)  
 Figure 6 (a) Unisoku UHV low-temperature STM (USM 1500S) system. The controllers for this system are shown in (b) and (c).

### 2.1.3.1 Chambers

The USM 1500S system includes four UHV chambers: the load lock (L) chamber, preparation (P) chamber, exchange (E) chamber, and STM chamber. Valves separate each chamber, allowing pumps to work in specific environments to their most efficient capacity. The samples are first loaded into the L chamber using a transfer rod. The L chamber is pumped down to low  $10^{-8}$  torr using the combination of a dry pump and a turbo pump (described in section 2.1.3.2), then moved into the P chamber using a magnetic transfer rod. The P chamber is generally kept below  $2 \times 10^{-10}$  torr, and it is the location where samples can be sputtered, annealed, and deposited onto. The E chamber is between the P chamber and the STM, and it also usually has a pressure below  $2 \times 10^{-10}$  torr. The main purpose of the E chamber is to transfer samples from the P chamber into the STM and vice versa. The E chamber can also be used for deposition experiments and tip/sample storage.

The STM chamber is connected to the E chamber and encircled by the refrigerator, as shown in Figure 7. The STM tip is below the sample stage and actually points upward. Due to the fact that samples are often moved in and out of the STM, it is convenient for the sample to be more accessible than the tip. Thus, the sample stage is above the tip and the sample faces down.

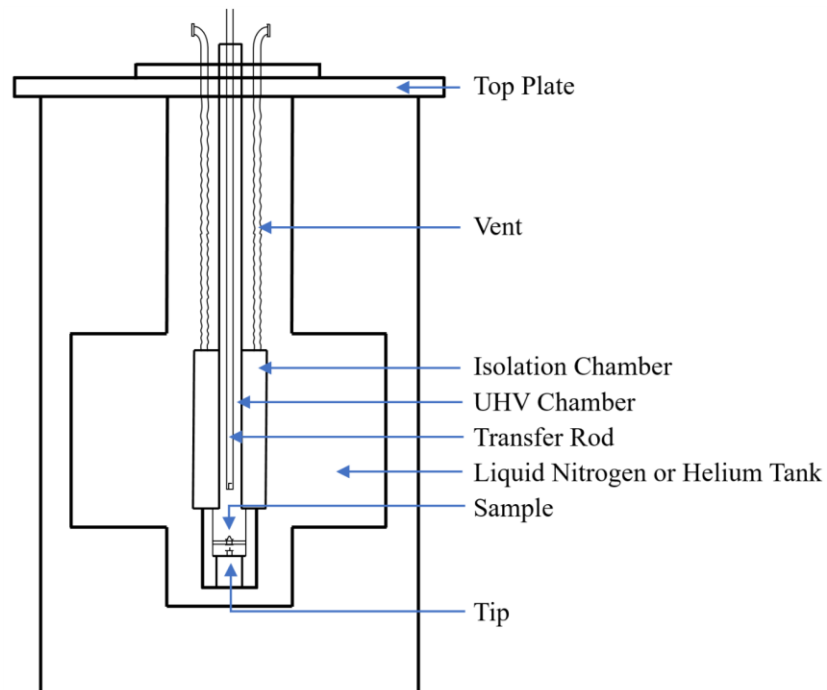


Figure 7 Schematic of the refrigerator and STM chamber <sup>22</sup>

### 2.1.3.2 UHV System

Several different pumps work together to maintain the UHV condition. The most robust pump is the mechanical dry pump. This pump is always utilized first to remove the bulk of the gas molecules in the chambers. On its own, the mechanical pump can get the vacuum levels into the  $10^{-3}$  torr range, though it is usually used in conjunction with a turbo pump. The turbo pump is directly attached to the L chamber, and it uses a series of high-speed fans to create a pressure differential within the pump itself. This differential sucks residual gas molecules into a region where the mechanical pump can remove them easily. With the turbo pump on, the pressure can get to  $10^{-9}$  torr.

The P and E chambers each have their own combination pump (ion pump plus titanium sublimation pump (TSP)). The ion pump emits an ion current into the pump volume where gas molecules are attracted to the ions and buried in the electrodes. The gas molecules are thereby removed from the chamber and the overall pressure decreases to  $10^{-10}$  torr. Occasionally, TSPs can be used to further decrease the pressure by heating Ti filaments to the point of evaporation. These Ti atoms deposit onto the inner surface of the chambers in the form of clean Ti (which is very reactive), trapping remaining atoms to the walls. TSPs are used sparingly since the heavy use of TSP will coat the inner surface of the UHV chambers with Ti, which negatively affects the cleanness of the chambers.

The mechanical pump and the turbo pump contribute a large amount of noise to the scanning environment, so they are only used as required. Conversely, the ion pumps are quiet, so they are kept running constantly.

Pressures are monitored using ion gauges. Each chamber has its own ion gauge connected by cables to the gauge controllers. To improve the longevity of the filaments, the sensors are disengaged above  $10^{-5}$  torr.

### 2.1.3.3 Cooling

When attempting to achieve atomic resolution, thermal noise can be a big issue. More heat contained in a system corresponds to more vibrational energy in each atom. The resulting

vibrations and thermal expansion drift can greatly decrease the quality of the STM images. To prevent this, the STM is surrounded by a cryostat capable of containing liquid nitrogen or liquid helium. Generally, liquid nitrogen is adequate for obtaining high-quality images with low drift and low thermal noise. The liquid nitrogen keeps the scanning environment at approximately 77 K (-196°C). Liquid helium would bring that temperature down to about 4 K (-269°C).

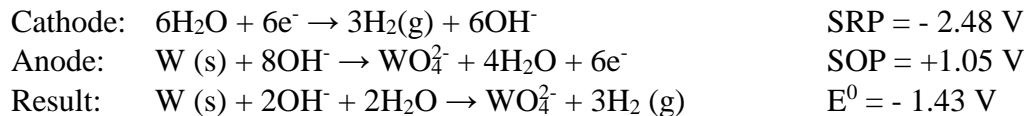
#### 2.1.4 STM Tips

The probe used for scanning is an important part for STM measurements. Dozens of tip materials and a variety of etching methods have been shown to be effective for STM scanning. Some of the more commonly used tips are shown in Table 2.<sup>23</sup>

*Table 2 Tip etching solutions and conditions*<sup>23,24</sup>

<b>Materials</b>	<b>Polishing Solution</b>	<b>Conditions</b>
Aluminum	10% perchloric acid in methanol	AC: a few V
Chromium	5 M NaOH aq. sol.	DC: a few V
Copper	Conc. H <sub>3</sub> PO <sub>4</sub>	DC: a few V
Gold	HCl (50%) + HNO <sub>3</sub> (50%) 20% KCN aq. sol.	AC: a few V AC: 10 → 3 V
Iridium	Molten NaNO <sub>3</sub> (3) + KOH(7) or NaCl 20% KCN aq. sol.	AC: a few V AC: 10 → 3 V
Molybdenum	NH <sub>4</sub> OH aq. sol. (8) + conc. KOH(2) Conc. KOH	AC: a few V DC: a few V
Nickel	40% HCl	AC: a few V
Platinum	Molten NaNO <sub>3</sub> (4) + NaCl(1) 20% KCN aq. sol.	DC: a few V
Tantalum	Molten NaNO <sub>2</sub> or KOH HF(2) + CH <sub>3</sub> COOH(0.5) + H <sub>3</sub> PO <sub>4</sub> (1) + H <sub>2</sub> SO <sub>4</sub> (1)	AC: ~8 V DC: 5-15 V
Tin	HF	AC: a few V
Titanium	HF	DC: 4 to 12 V
Tungsten	Same as molybdenum	
Zinc	Conc. KOH	DC: 10 to 15 V
Zirconium	10% HF	Dip into solution

Electrochemically etched tungsten (W) tips are used in this work. The tips start simply as W wires with a diameter of 0.375 mm. The solution for tip etching is 2 M NaOH solution (4.8 g NaOH plus 60 mL deionized water). A bit of W wire is submerged vertically into the solution along with a stainless-steel rod. These metals act as the anode and cathode, respectively, when attached to a DC power supply. A voltage is applied between the two electrodes, causing an exchange of electrons near the surface of the solution.



This chemical reaction dissolves the W wire at the liquid-air interface (the shortest distance for the electron exchange), causing a bottleneck to form (Figure 8).<sup>25</sup> Eventually, the portion of wire suspended in the solution drops away, ideally leaving a single-atom pointed tip left over. This tip is cleaned with deionized water and isopropyl alcohol before being placed into a tip holder.

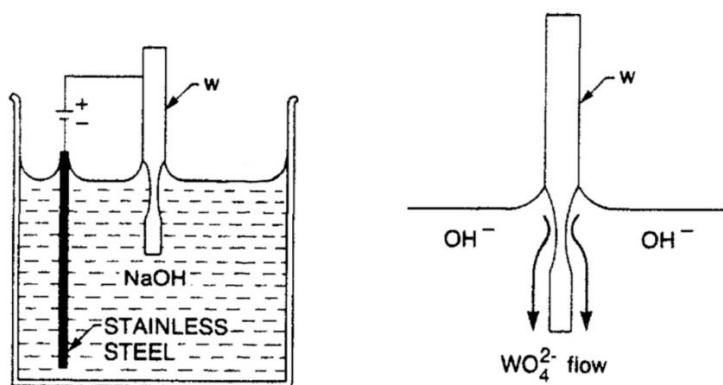


Figure 8 Schematic of the DC etching method for tip preparation<sup>20</sup>

A similar setup can be used with alternating current, which will produce a much blunter tip. Fine etching can then be performed under an optical microscope to sharpen the tip. The shape of the tip obtained by DC etching is different from that obtained by AC etching, as shown in Figure 9.

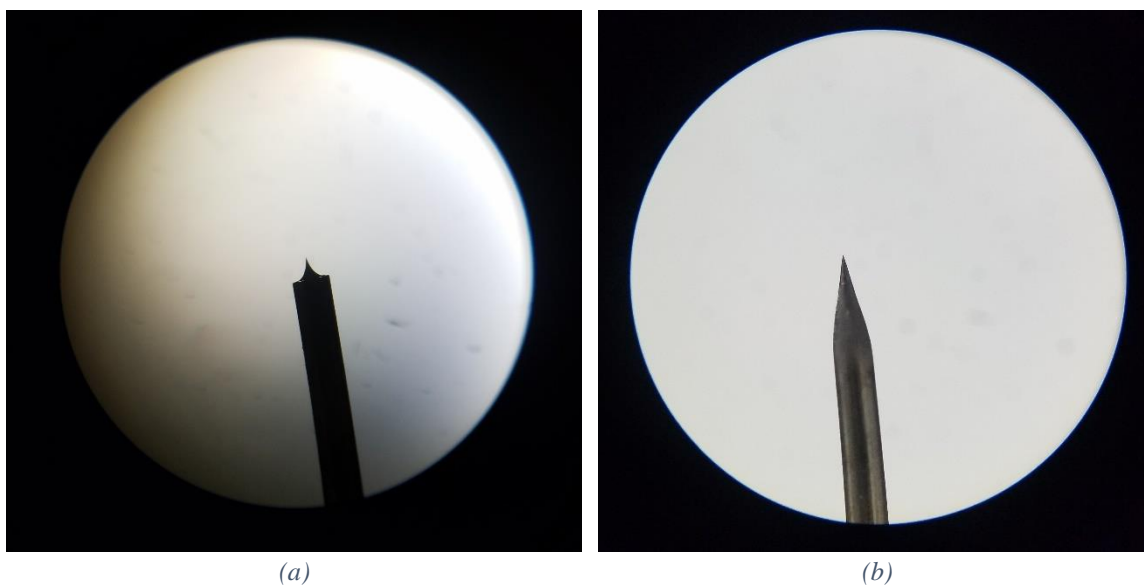


Figure 9 W tips prepared by (a) DC etching and (b) AC etching (Magnification: 40×)

Sharpness is incredibly important for the STM tip to produce high spatial resolution. The angle at which the W wire is submerged into the solution, the vibrational stability of the liquid surface, the chemical and electrical parameters, and the time taken to etch can all affect the tip sharpness.

The state of the tip can change during scanning. As the tip moves across the sample surface, it may be prone to picking up or dropping off atoms. This sometimes leads to the formation of multiple tips which would produce misleading STM images. When this happens, it is necessary to pulse the tip with a high bias voltage to induce further changes to the tip until it reverts to a sharp single tip.

The worst thing that can happen to a tip when scanning is physical contact with the sample. This is known as “crashing” the tip. In addition to scratching the sample, there is a high probability that the tip will be destroyed. Precautions are taken to avoid this. When approaching the tip to the sample, an auto-approach method can move the tip with incredibly fine increments until a target set-point current is reached. Additionally, we always scan in constant-current mode. Constant-height mode can be dangerous for the tip if the surface details are not known, since the tip can crash into an unseen elevated point on the sample surface.

#### 2.1.5 Molecular Evaporator

A molecular evaporator is used to deposit molecules onto the sample in the P chamber. The molecules (usually in powder form) are placed into a ceramic crucible with a W filament surrounding it. The filament is heated with DC power, imparting energy to the molecules. Once a target evaporation temperature is reached (Figure 11), a shutter in the P chamber is opened allowing the energetic molecules to evaporate into the chamber and onto the sample. The surrounding parts of the evaporator are water cooled.



Figure 10 Molecular evaporator (a) by itself<sup>26</sup> and (b) installed to the P chamber

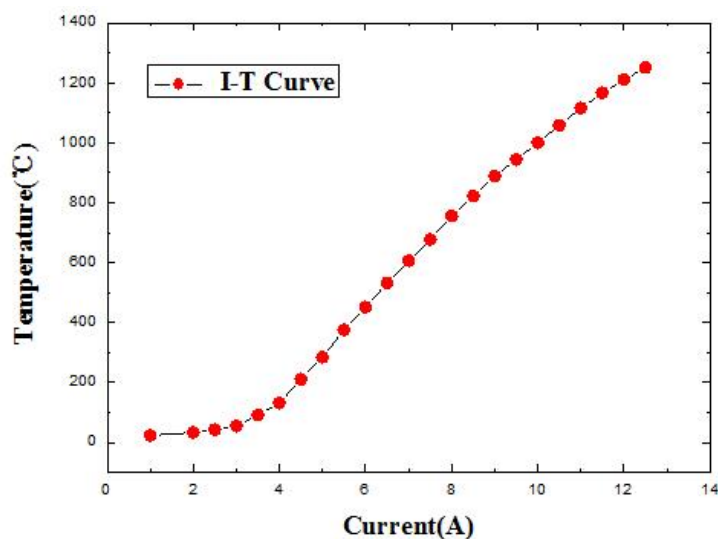
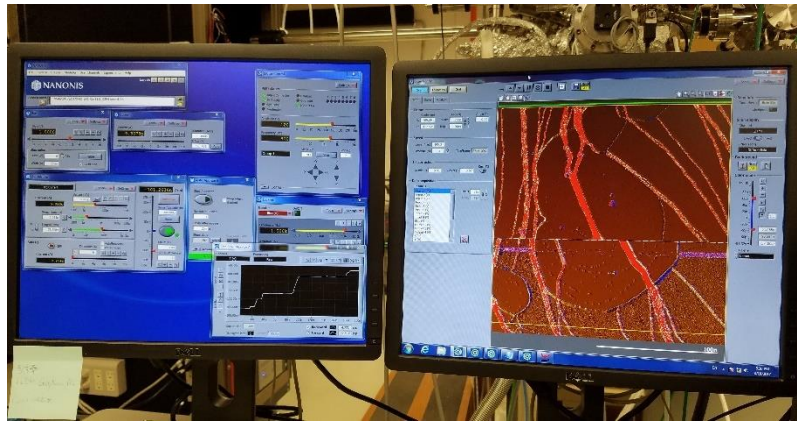


Figure 11 Crucible temperature versus filament current for the molecular evaporator<sup>26</sup>

### 2.1.6 Data Acquisition

The current signal obtained during scanning is amplified using a FEMTO pre-amplifier placed between the STM and the Nanonis controllers (set to a gain of  $10^9$  V/A for the measurements in this work). Nanonis software, built on LabVIEW, is the primary software used for our experiments. Features of the software include tip approaching, bias voltage and set-point current adjustment, scanning and saving images, tilt correction, noise analysis, spectroscopy, and so on.



*Figure 12 Data acquisition using Nanonis software*

### 2.1.7 Spectroscopy

Scanning tunneling spectroscopy (STS) measurements are conducted at specific locations on a sample to determine electrical properties at those points. In most cases, STS measurements must be done at many locations in order to compare points of interest. For example, we may be curious about dopants, effects of dopants on areas immediately surrounding the dopants, areas far away from the dopants, and the substrate itself.

STS requires us to first position our probe over the region of interest. At that point, we must fix the tip height by setting a bias voltage and set-point current. This parameter is important for acquiring a good signal-to-noise ratio (SNR). If the tunneling current is too low, noise will dominate the measurement. If it is too high, the STS process can physically change the sample surface or tip. It could also lead to oversaturation of the current signal.

Once a sample-tip separation height is found to produce a good SNR, we must then specify our voltage range for sampling. These ranges adequately surround the Fermi energy such that low energy trends may be evaluated (for example, -1.2 V to +1.2 V or -3 V to +3 V).

The final parameters to set are the modulation frequency, modulation amplitude, the number of steps within our voltage range that we would like to test, and the number of sweeps to conduct (more sweeps smooth out our eventual graph of the data by averaging).

At each DC step within our voltage range, a small AC voltage is applied. This voltage causes a slight change in the tunneling current. The  $dI/dV$  ratio can be plotted as a function of voltage in order to produce STS plots. The equipment can also record lock-in values (proportional to  $dI/dV$ ), raw current values, and energy in eV.

Line spectroscopy may also be measured using our STM. In this case, point spectroscopy is conducted as described above at many locations along a line spanning some interesting space. The output is in the form of many individual  $dI/dV$  versus voltage (or energy) curves, which can then be plotted into a two-dimensional figure, as shown in Figure 13(b).

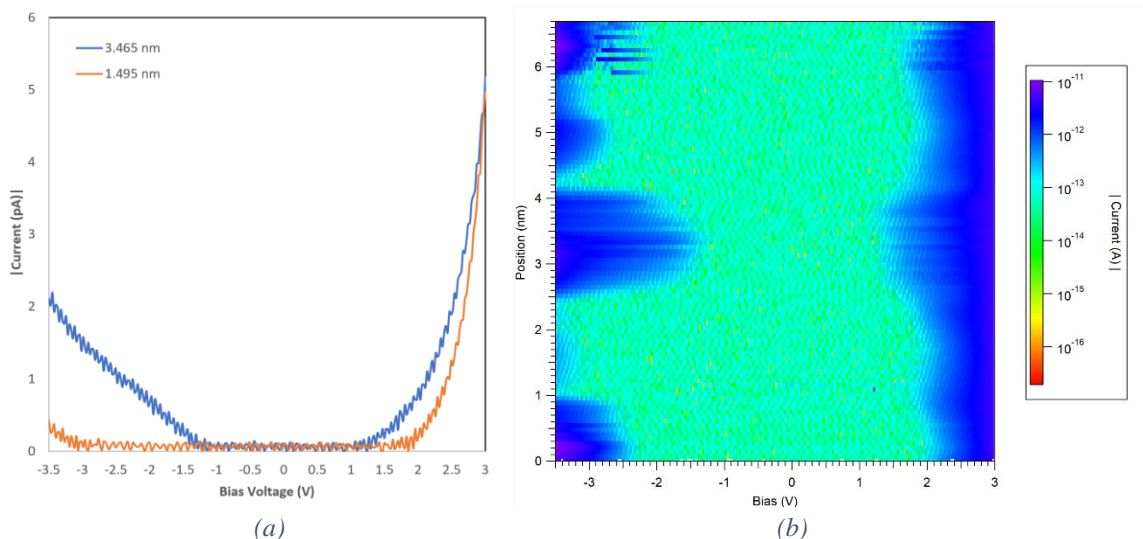


Figure 13 Examples of (a) point spectra and (b) line spectra recorded on  $TiO_2(001)$

## 2.2 X-ray Photoelectron Spectroscopy

The first commercial XPS instrument was developed in 1969.<sup>27</sup> One of its inventors, Kai Siegbahn, won the Nobel Prize in Physics in 1981 for its invention.<sup>27</sup> XPS spectra provide the ability to identify and quantitate which elements are present on a sample and the binding energies of various electron states. Thus, chemical analysis from the XPS is an important complementary technique to the STM.

### 2.2.1 Principles

To obtain an XPS spectrum, the sample is exposed to soft X-rays causing photoelectrons to be ejected. The kinetic energy of those photoelectrons is measured and the electrons are counted to produce a graph of number of electrons versus electron energy. Peak areas in

the graph are used to calculate the atomic concentrations of elements on the surface since the kinetic energy of electrons from each element will be different for given X-ray energy.<sup>27</sup>

### 2.2.2 Theory

XPS takes advantage of the photoelectric effect to ionize substrate atoms. As shown in Figure 14, X-rays irradiate the substrate, adding energy equal to  $h\nu$  to the core electrons and “kicking” those electrons, called photoelectrons, out. Since the energies of the set of orbitals for every atom are unique, different types of atoms will eject electrons with different kinetic energies,  $E_K$ . By measuring  $E_K$ , we can determine the binding energies,  $E_B$ , of the component atoms, providing us with a comprehensive chemical analysis of the substrate. The equation used is  $E_B = h\nu - E_K - \Phi$ , where  $\Phi$  is a work function.<sup>28</sup> For the XPS, the work function is a limiting factor. Photons with  $h\nu < \Phi$  (about 3-4 eV) are too energetically weak to cause photoemissions.

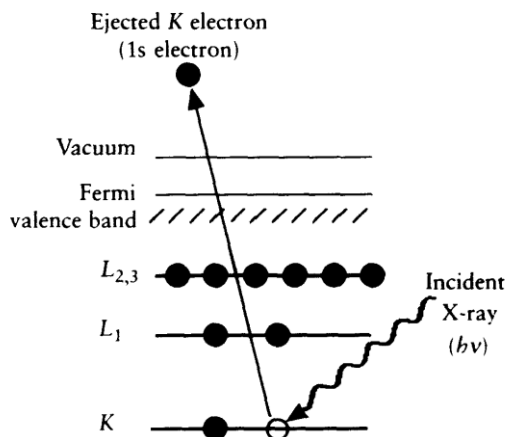


Figure 14 Schematic of the photoemission process in XPS<sup>28</sup>

There are many X-ray sources that can be used for XPS, as seen in Table 3. The two most commonly used sources are the Al and Mg K $\alpha$  emissions.<sup>29</sup> The sources are not perfectly monochromatic. Monochromatic sources are ideal for narrowing output peak widths, though methods of achieving this will result in decreased intensity.<sup>29</sup> Also illustrated in Table 3 is the relationship between energy and full-width half maxima (FWHM). Though anode sources with higher energies increase the number of electron states available to be excited by the X-rays, the resulting XPS spectrum will generally contain broader peaks. This makes element matching more difficult and increases the risk of blending two or more peaks with similar binding energies.

Table 3 XPS anode materials<sup>28</sup>

Element	Line	Energy (eV)	Full-width half maximum (eV)
Y	Mζ	132.3	0.47
Zr	Mζ	151.4	0.77
Mg	Kα <sub>1,2</sub>	1253.6	0.7
Al	Kα <sub>1,2</sub>	1486.6	0.9
Si	Kα	1739.6	1.0
Zr	Lα	2042.4	1.7
Ag	Lα	2984.4	2.6
Ti	Kα	4510.9	2.0
Cr	Kα	5417.0	2.1

The X-ray anodes are bombarded with electrons from heated W filaments, creating core holes in the anode atoms and generating X-rays through X-ray fluorescence. The X-rays are directed towards the sample in UHV. UHV allows the emitted electrons to travel into the detector without interacting with air molecules. Although the X-rays can penetrate tens of microns into the sample, the photoelectrons emitted by the atoms only travel 3-30 nm. Consequently, the atoms near the surface of the sample will produce the dominant number of photoelectrons detected.

Emitted photoelectrons travel first through an electrostatic lens then into a curved region between two hemispheres before reaching the detector (Figure 15). The electrostatic lens focuses the photoelectrons into an aperture leading to the hemispheres. The potential difference in the hemispheres creates an electric field which deflects the electrons along a curved path. Electrons with energies too high or too low will over- or under-deflect, resulting in contact with the hemispheres and no detection. The electrons that get through have energy  $E_K = e\Delta V \left( \frac{R_1 R_2}{R_2^2 - R_1^2} \right)$  where  $e$  is the electron charge,  $\Delta V$  is the hemisphere potential difference,  $R_1$  is the inner hemisphere radius, and  $R_2$  is the outer hemisphere radius.<sup>28</sup> For a given apparatus, the radii will be known. Therefore, the potential difference directly determines the kinetic energy of the electrons arriving at the detector.

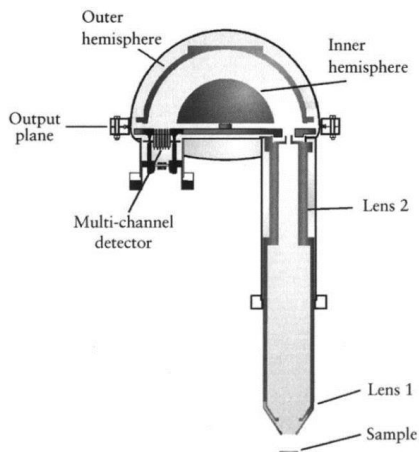


Figure 15 Design of the hemispherical energy analyzer<sup>28</sup>

By sweeping through potential differences in ranges determined by the source, we can map out the spectrum of kinetic energies of all electrons read by the detector. Those kinetic energies are converted into binding energies and cross-referenced with known binding energies to determine the chemical composition of the sample. Generally, elements with higher atomic numbers have greater nuclear attraction, so more energy is required to eject core electrons.

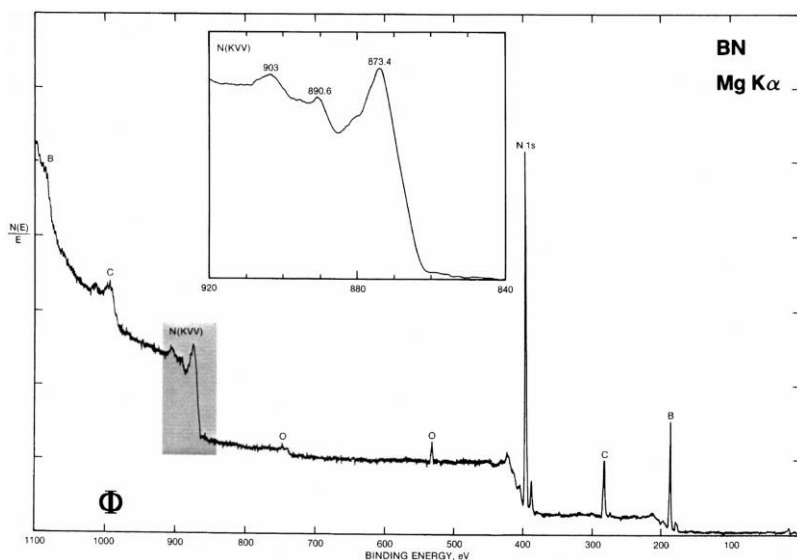


Figure 16 Example of an XPS spectrum for N<sup>30</sup>

The simple single-electron process described above tends to account for most of the detected electrons. However, a three-electron process involving Auger electrons can complicate the shape of the XPS spectrum. When incoming X-rays cause core electrons to be ejected, the vacancy in the core is energetically unfavorable. This can cause an electron

from a higher state to drop into the core level to fill the space. Energy is released by that electron in this process in the form of fluorescence, which can then cause a third electron (the Auger electron) to escape. Auger electrons are also read by the detector, and XPS spectra must account for them when analyzing the chemical composition of the substance.

Most of the notation seen in XPS is the chemistry convention for atomic orbitals (1s, 2s, 2p, etc.), but Auger electrons use physics notation (K, L, M, etc.) to describe the three-electron process. In Figure 16, the highlighted (and inset) region between 840 and 920 eV corresponds to Auger peaks. The letters KVV describe the energy levels of the emitted core electron, the electron that replaced it, and the electron that was ejected because of the replacement in that order.

### 2.2.3 Physical Electronics XPS

The XPS used for our experiment is a Physical Electronics 5200 XPS purchased in 1999. The X-ray sources are the common Al and Mg  $K\alpha$  emissions with no additional monochromation. As described previously, W filaments are heated as the source anodes are biased to 15 kV. Electrons from the filament strike the anodes, causing the Auger process and X-ray fluorescence to occur. The anodes are water cooled during this process, and the X-rays they release are collimated and directed toward the sample.

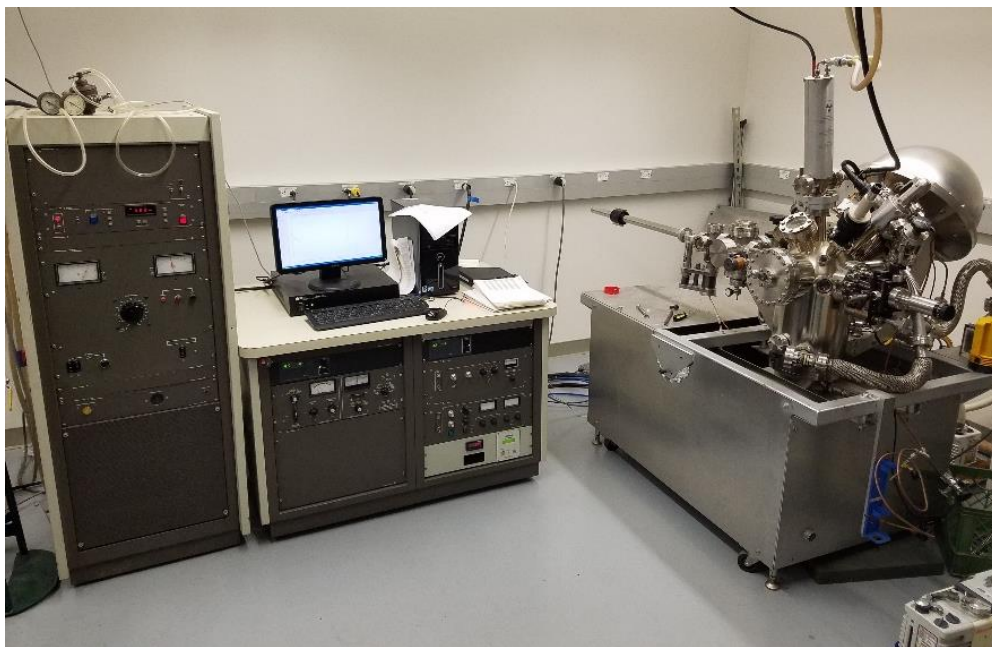


*Figure 17 XPS system and its controller*

There are two main chambers in the XPS. An airlock (similar to the STM's L chamber) is used for loading the sample and acts as an initial pumping stage. A turbo pump connected to this chamber maintains the pressure at about  $10^{-8}$  torr. An ion pump connected to the main analysis chamber maintains the pressure at  $10^{-10}$  torr. Samples are moved within the chambers using magnetic transfer rods.

#### 2.2.4 Data Acquisition

XPS data is acquired by sweeping the hemispheres through a range of potentials and counting the number of electrons detected as a function of this voltage differential. The detector uses an electron multiplier to create a readable current. The current is converted to a binary signal, and the number of counts per unit time is what eventually gets graphed against the binding energy. AugerScan software graphs this information by scanning the voltages several times and averaging the results.

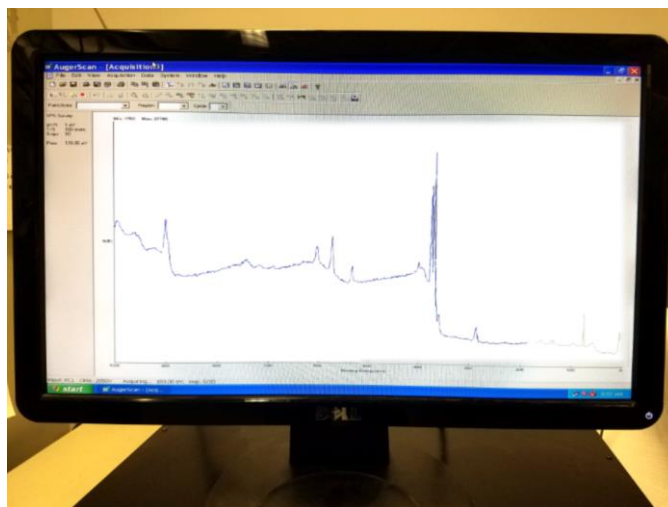


*Figure 18 Data acquisition for the XPS*

The peaks are matched with known data from a handbook to identify the elements and their orbitals. Confidence in the matching process is increased when multiple peaks from single elements can be identified.

#### 2.2.5 Sample Transportation

The STM lab and XPS lab are next to each other, which requires only a short exposure time for the sample in air (less than 15 minutes) during the transfer from the STM to the XPS system.

### 3 Nitrogen-Doped Graphene on Cu(111)

#### 3.1 Sample and Precursor

The Cu(111) sample was purchased from Princeton Scientific and customized to our specifications. The polished surface of the sample is 4 mm by 4 mm. It was grown using the Czochralski method and is 99.999% pure. Its orientation accuracy is less than  $0.1^\circ$ .

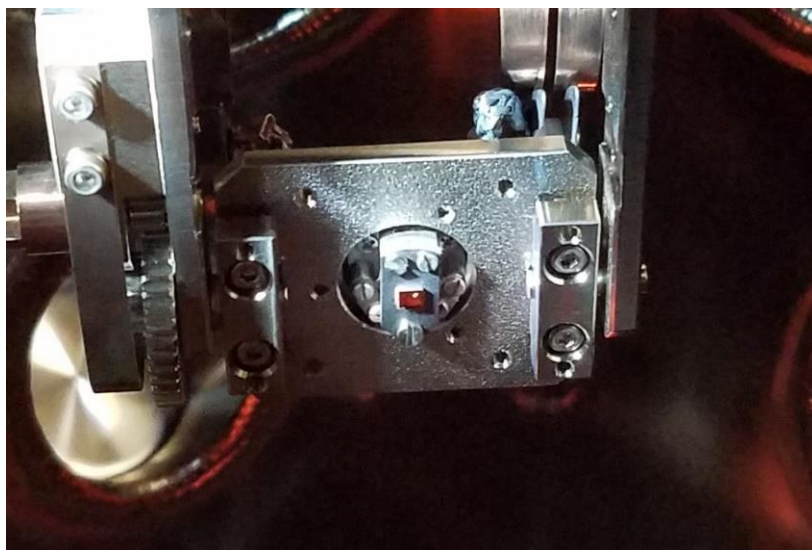


Figure 19 The Cu(111) sample in the preparation chamber

The  $C_{59}NH$  molecules were prepared by Prof. Liangbing Gan's lab at Peking University. The process involved chemical treatment of a fullerene-mixed peroxide molecule, as shown in Figure 20.<sup>31</sup> The resulting azafullerene molecule contains hydrogen, and may contain residual solvents as impurities. These impurities are evaporated from the molecule with sufficient energy, as in the outgassing process before the molecules are deposited onto the sample. Nuclear magnetic resonance spectrometry was unable to detect other impurities, indicating that the molecules are above 99% pure.<sup>13</sup>

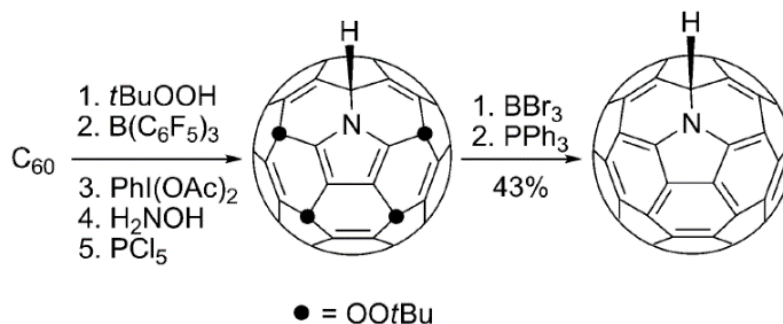
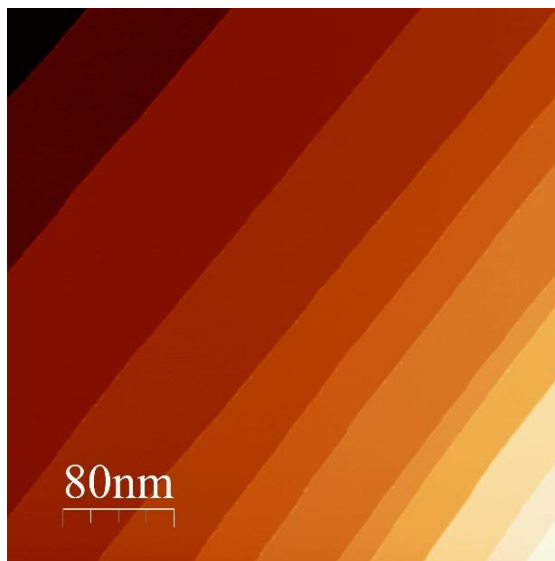


Figure 20 Synthetic chemistry of the  $C_{59}NH$  molecule<sup>31</sup>

### 3.2 Preparation

Once in our lab, the Cu(111) sample was first submerged in 1 M of HCl for one hour, then cleaned ultrasonically in deionized water, acetone, and finally isopropyl alcohol. The HCl removes oxide layers from the surface, and the other solutions take care of most other impurities.

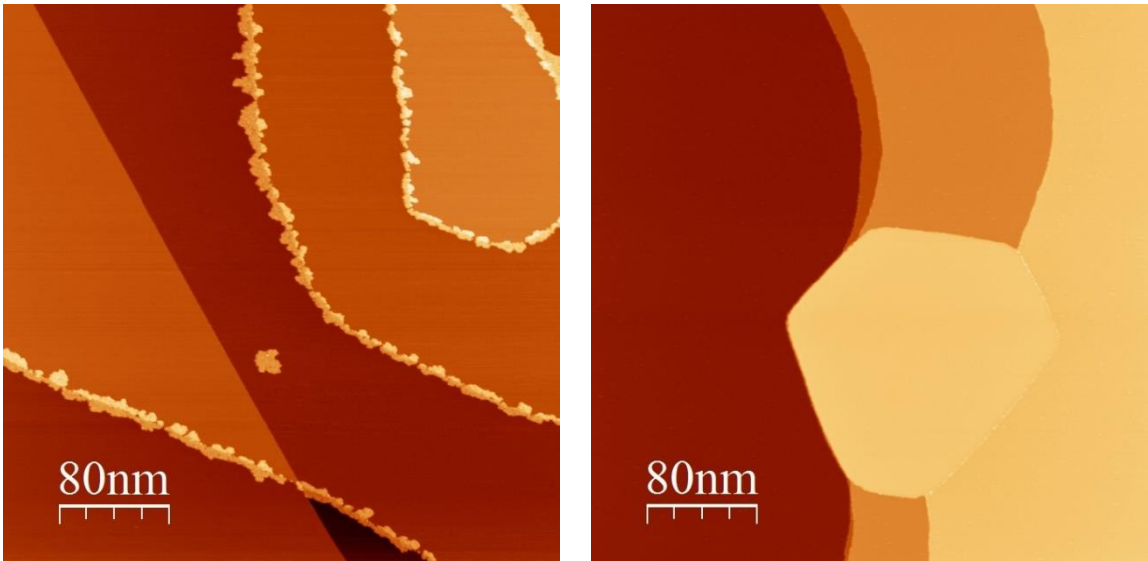
The sample was further cleaned using repeated cycles of Ar<sup>+</sup> sputtering (1.5 keV at  $1.0 \times 10^{-5}$  torr for 15 minutes each at two oblique angles) and annealing (600°C for 30 minutes). The sample temperature was measured using an IMPAC IGA 8 Pro pyrometer. The emissivity was set at 10% for Cu(111) for our experiments. The sample was periodically checked with the STM until it was clean.



*Figure 21 STM image of clean Cu(111) surface  
Size: 400 nm × 400 nm; Scanning Parameters: 3 V, 50 pA*

### 3.3 Synthesis

Once the Cu(111) sample was cleaned, the C<sub>59</sub>NH molecules were heated to 330°C and deposited onto the sample surface for one hour (Figure 22(a)). Following the deposition, the sample was progressively annealed from 400°C to 700°C in 100°C increments and held at each step for 5 minutes (Figure 22(b)). The total annealing time was approximately 30 minutes. Subsequent STM scans showed that this temperature was sufficient for decomposing the molecules and forming graphene.



(a) *STM image before annealing showing the  $C_{59}NH$  molecules adsorbed on the Cu(111) surface.*  
 Size: 400 nm  $\times$  400 nm; Scanning Parameters: 3 V, 10 pA

(b) *STM image after annealing showing the formation of graphene on the Cu(111) surface.*  
 Size: 400 nm  $\times$  400 nm; Scanning Parameters: 3 V, 5 pA

At low coverages, identifying dopants is difficult due to their rarity. Identical deposition and annealing cycles were conducted and the sample periodically scanned until the graphene was near one complete monolayer (see Figures 25, 26, and 27 below).

The doping was investigated and scanned with atomic resolution. The dark spots seen in many of the following STM images can be attributed to carbon monoxide (CO) adsorbates on the Cu(111) surface. CO is a common surface defect which can be identified and accounted for by comparing images scanned at different biases. Since the CO molecules are on the Cu surface rather than in the graphene lattice, they are not a point of emphasis in this research.<sup>32,33</sup>

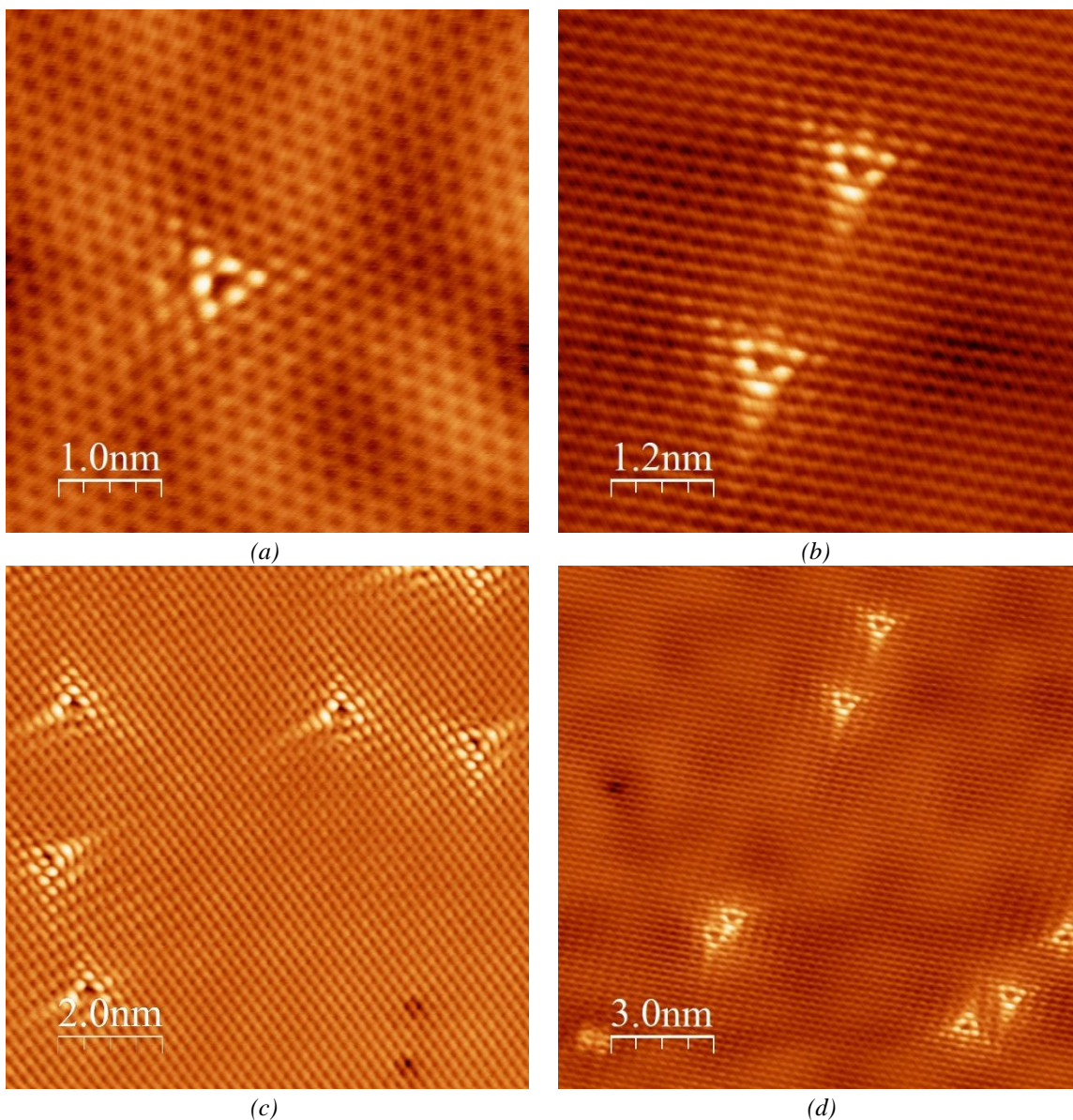


Figure 23 Atomic-resolution STM images of graphene with N dopants.  
 (a) Size: 5 nm × 5 nm; Scanning Parameters: 10 mV, 3 nA  
 (b) Size: 6 nm × 6 nm; Scanning Parameters: 10 mV, 3 nA  
 (c) Size: 10 nm × 10 nm; Scanning Parameters: 20 mV, 2 nA  
 (d) Size: 15 nm × 15 nm; Scanning Parameters: 10 mV, 3 nA

The STM images of the dopants suggest that, within graphene islands, the predominant doping configuration is graphitic N.<sup>34</sup> This is when a N atom replaces a C atom in the graphene lattice. In Figure 23, the N atoms are the dark spots in the middle of each triangle, and the surrounding C atoms are brightly contrasted. This is consistent with previous research.<sup>34</sup> Illustrated in Figure 24(a) are several possible types of N-doping in graphene.

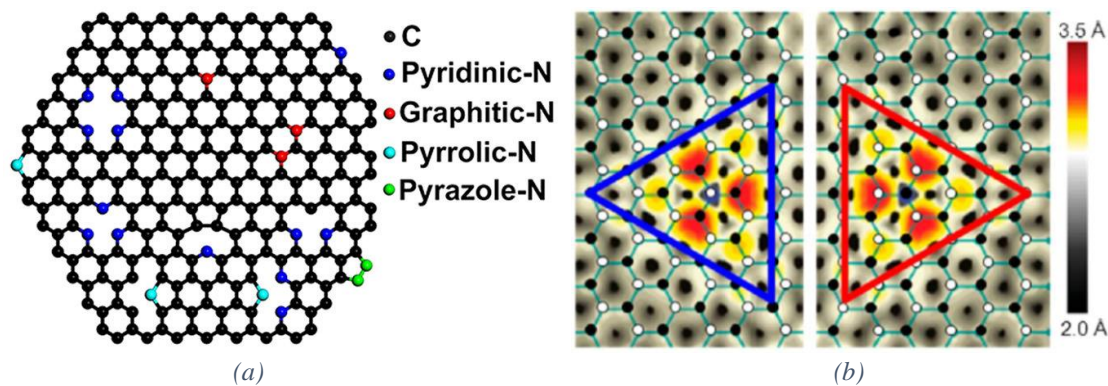


Figure 24 (a) Typical N-doping configurations in graphene<sup>34</sup> (b) Graphitic N on A and B atom<sup>35</sup>

As shown in Figure 24(b), there are two orientations for the dopant features depending on whether the graphitic N replaces the A or B atom in the graphene lattice.<sup>36</sup> This is exactly what we observe with the dopants in each of our scans. In our experiments, the two orientations seem to appear randomly.

The next step in our research was to study how the distribution of doping changes with repeated cycles of deposition and annealing. Images were taken between each cycle to attempt to quantify the change. Figures 25, 26, and 27 reveal the progression (see Supporting Information section for the method used to calculate the fraction of graphene coverage). The final doping concentration was compared to earlier depositions and found to have increased in general.

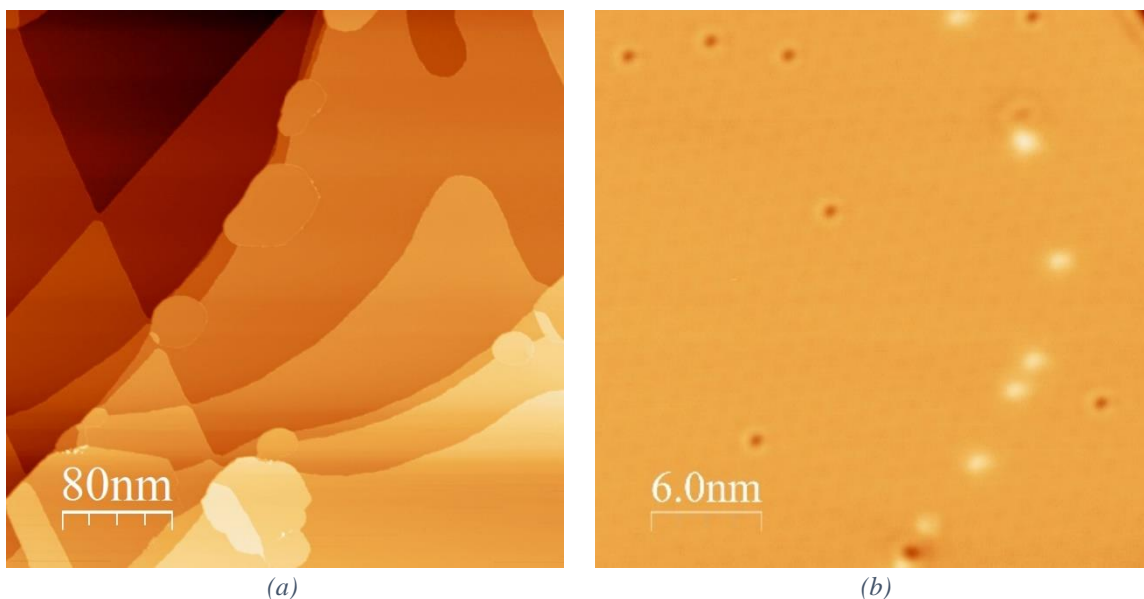
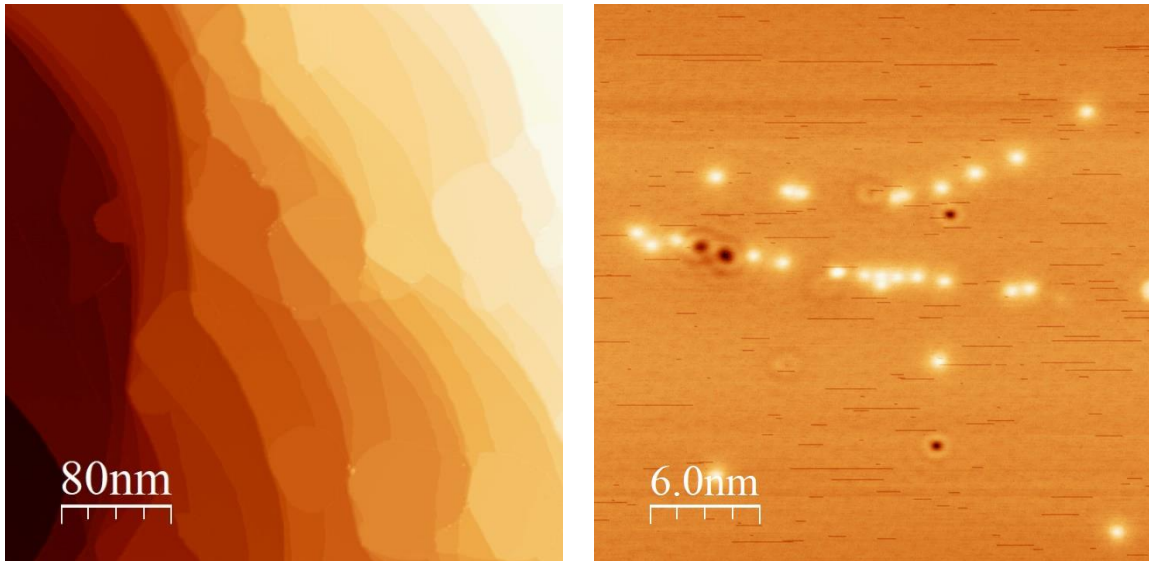
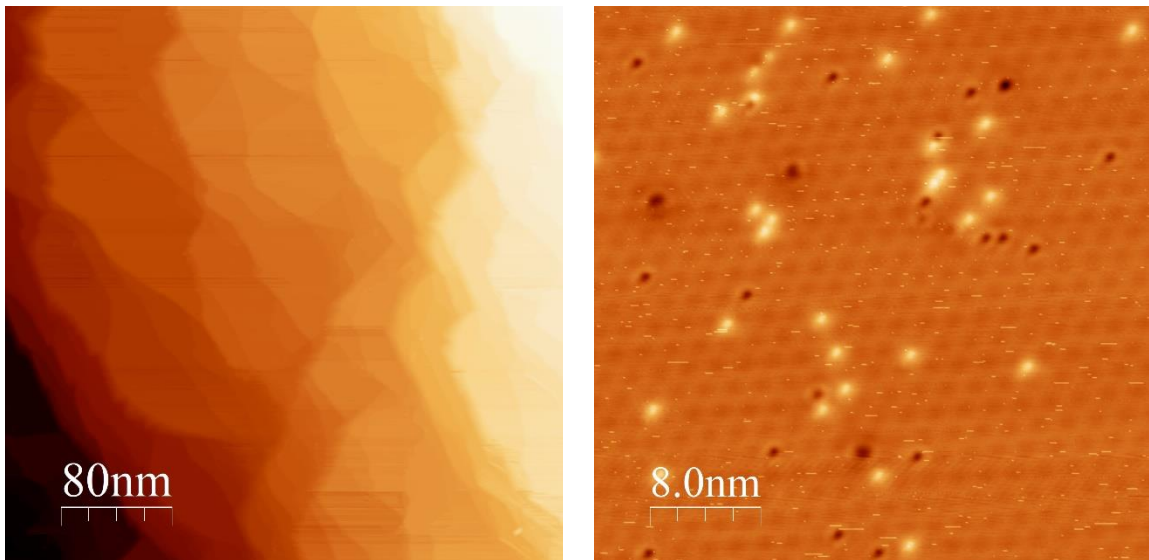


Figure 25 STM images of 0.14 ML N-doped graphene on Cu(111)  
 (a) Size: 400 nm × 400 nm; Scanning Parameters: 3 V, 50 pA  
 (b) Size: 30 nm × 30 nm; Scanning Parameters: 1 V, 10 pA



(a) (b)  
 Figure 26 STM images of 0.35 ML N-doped graphene on Cu(111)  
 (a) Size: 400 nm × 400 nm; Scanning Parameters: 3 V, 10 pA  
 (b) Size: 30 nm × 30 nm; Scanning Parameters: 1 V, 10 pA



(a) (b)  
 Figure 27 STM images of 1.0 ML N-doped graphene on Cu(111)  
 (a) Size: 400 nm × 400 nm; Scanning Parameters: 3 V, 10 pA  
 (b) Size: 40 nm × 40 nm; Scanning Parameters: 1 V, 50 pA

### 3.4 STM Results

There was a novel behavior observed with the doping. We noticed after several cycles that the dopants tended to arrange themselves into curved lines (Figure 28). This is why certain regions tended to be more heavily doped than other regions.

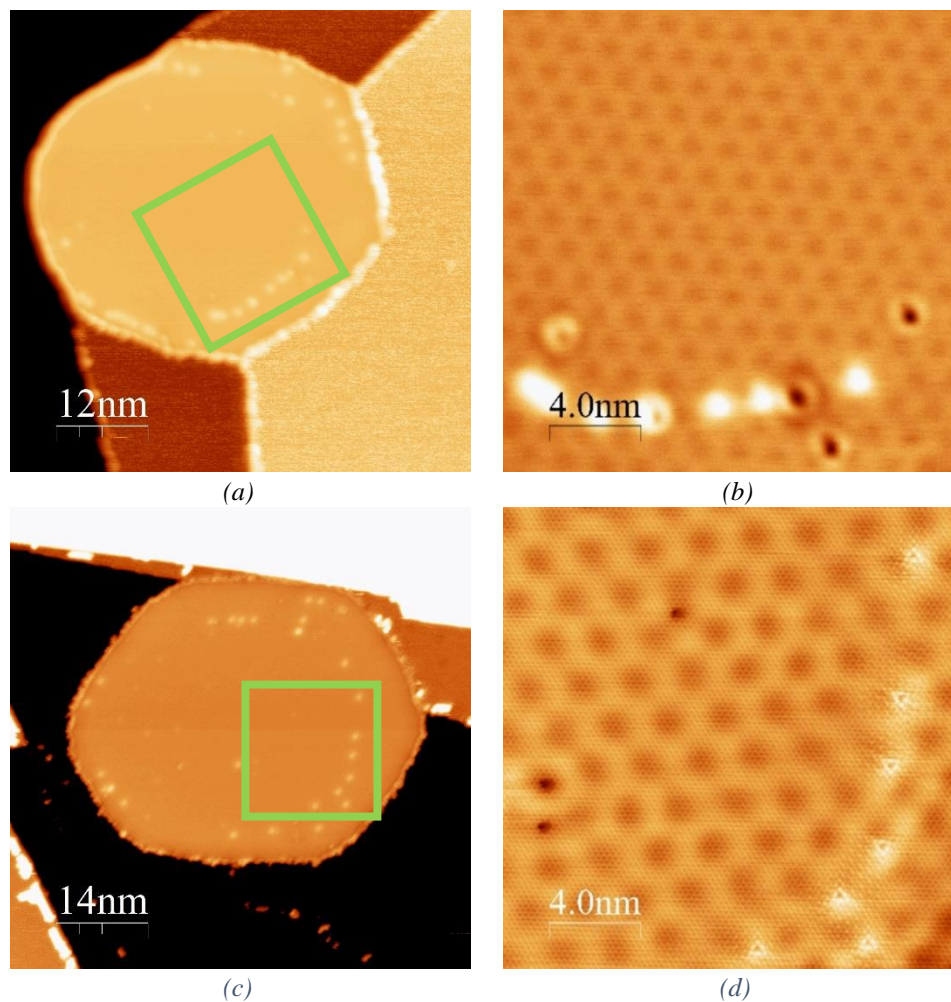


Figure 28 Two examples of dopant alignment along graphene edges  
 (a) Size: 70 nm × 70 nm; Scanning Parameters: 3 V, 10 pA  
 (b) Size: 20 nm × 20 nm; Scanning Parameters: 1 V, 10 pA  
 (c) Size: 60 nm × 60 nm; Scanning Parameters: 3 V, 10 pA  
 (d) Size: 20 nm × 20 nm; Scanning Parameters: 20 mV, 5 nA

Further cycles of molecule deposition and annealing showed that the dopants form rings, as shown in Figure 29. One possible reason for the formation of rings is that N atoms prefer to bond to graphene edges during graphene growth, and the N atoms on the edge of a graphene island form a ring of graphitic N atoms in the next growth cycle.

This discovery has interesting potential applications (discussed in chapter 4) and gives us deeper insight into graphene formation using this process. Counting the number of dopant rings acts as a method of “aging” the graphene islands. For example, an island with three dopant rings indicates that the graphene has been present for at least three cycles of

deposition and annealing. The shape of the rings is also an indication of how the graphene islands grew.

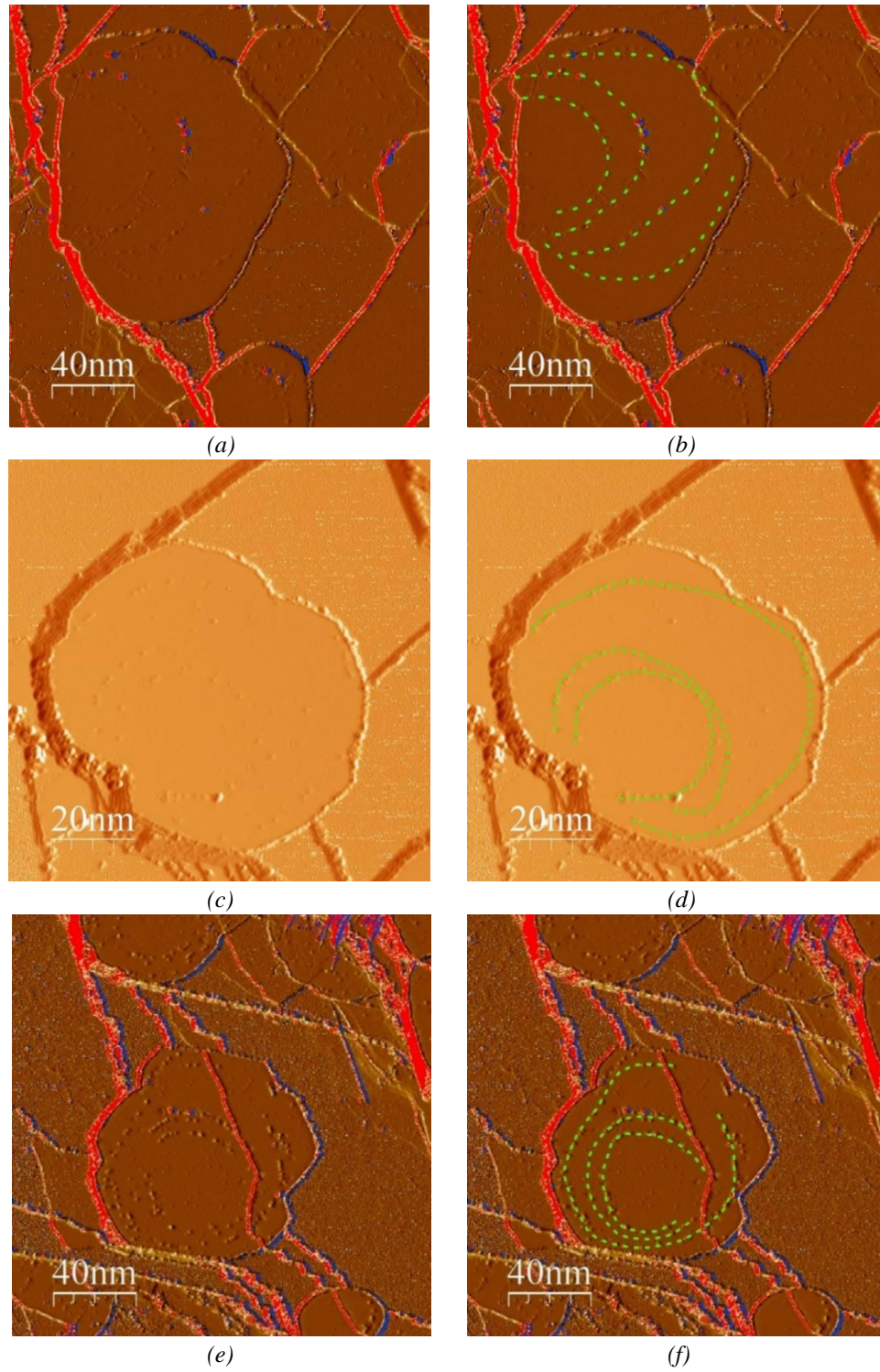


Figure 29 STM images showing the rings of N dopants on different graphene islands.

(a) Size:  $200\text{ nm} \times 200\text{ nm}$ ; Scanning Parameters: 1 V, 10 pA

(c) Size:  $100\text{ nm} \times 100\text{ nm}$ ; Scanning Parameters: 3 V, 10 pA

(e) Size:  $200\text{ nm} \times 200\text{ nm}$ ; Scanning Parameters: 3 V, 10 pA

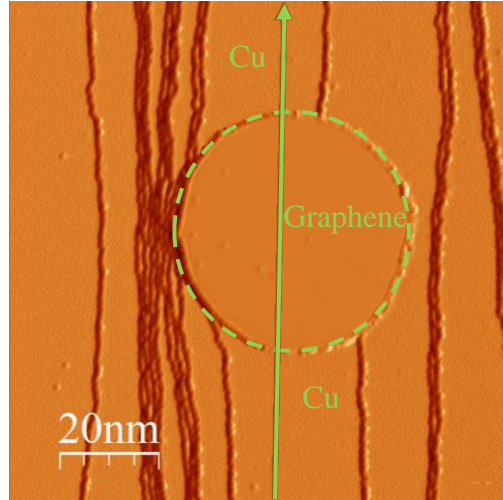
The islands shown in Figure 29(a), (c), and (e) were scanned after 7, 8, and 8 deposition and annealing cycles respectively. When using the dopant rings to determine the number of growth cycles since the formation of a graphene island, it is clear that the number of rings only gives us a lower limit. It is possible that a specific graphene island did not grow for several cycles or that some cycles did not contribute to the growth of the island. Figure 29(e) and (f), for example, shows a graphene island with at least three rings of graphitic N dopants. Therefore, we can state with some confidence that this island has been subjected to at least four cycles of deposition and annealing, but we cannot conclusively state that it has been present for exactly four cycles.

The shape of these rings gives us a history of the formation of the islands. It is clear that the islands do not grow symmetrically out from the center. If they did, the dopant rings would be in the form of concentric circles. The distance between the rings would be a predictable function of the molecule deposition time (holding other parameters fixed). Instead, we observe curved paths for the rings which indicates that the graphene islands can grow more rapidly in certain directions than others. This is likely due to preferred energy conditions related to the preexisting islands and the underlying Cu. It seems the island will tend to grow along the same or lower copper terraces instead of climbing to higher terraces.

The XPS of our sample was measured to confirm the chemical composition of the surface. The results are presented in section 3.6.

### 3.5 STS Data

Scanning tunneling spectroscopy was needed at various stages of the experiment to compare our results with previous experiments and to quantify changes in electrical properties.



(a)

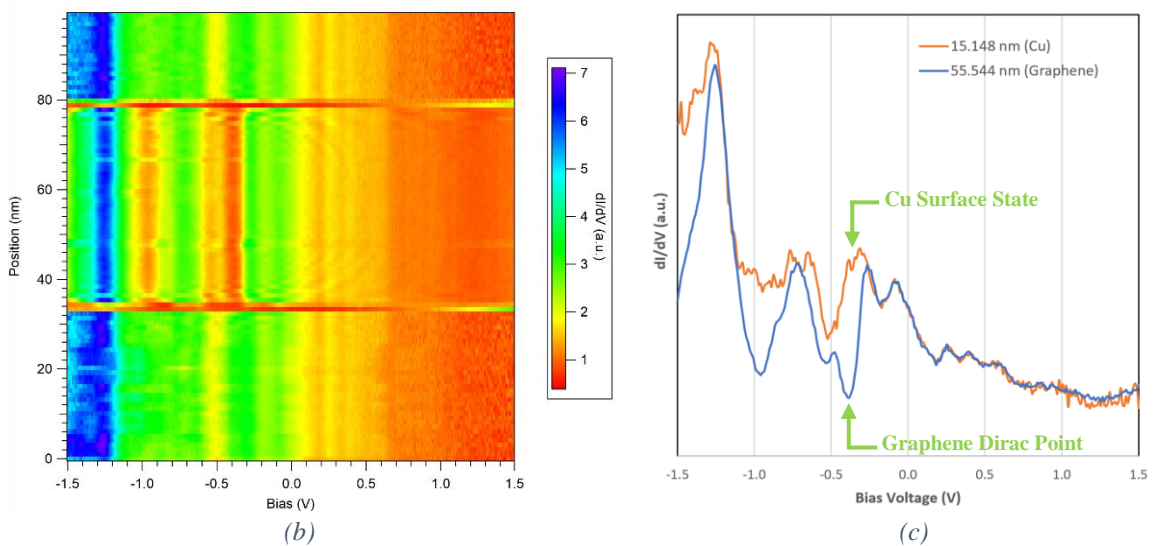


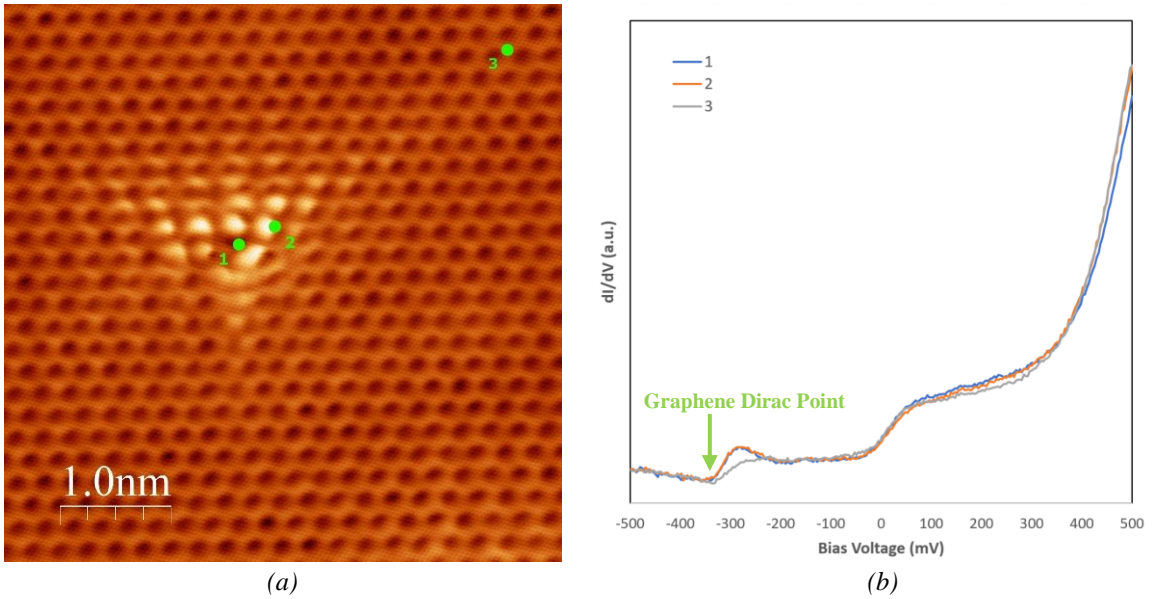
Figure 30 STS of N-doped graphene on Cu(111)

(a) Size:  $100 \text{ nm} \times 100 \text{ nm}$ ; Scanning Parameters: 2 V, 100 pA

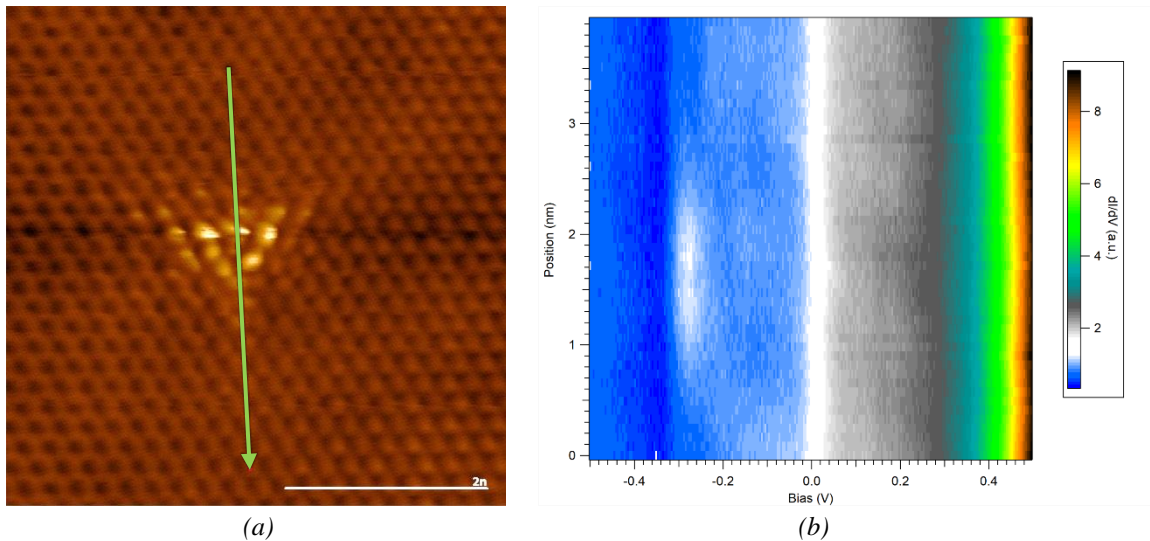
(b)  $dI/dV$  line spectra recorded along the green arrow in (a)

(c) Selected  $dI/dV$  point spectra recorded on Cu and graphene

Figure 30 shows the  $dI/dV$  line spectra recorded along a line (from Cu to graphene and back to Cu) in (a). The two-dimensional plot of the  $dI/dV$  line spectra clearly shows the difference in electronic structure between the graphene and Cu regions, as shown in (b). Two selected  $dI/dV$  point spectra are shown in (c). The dip at -400 mV on the  $dI/dV$  spectra of graphene can be attributed to the Dirac point. The shift of Dirac point from the Fermi level to -400 mV can be attributed to  $n$ -doping induced by the Cu substrate and the N dopants.



(a) (b)  
 Figure 31  $dI/dV$  point spectra of N dopant and surrounding C atoms  
 (a) Size:  $5\text{ nm} \times 5\text{ nm}$ ; Scanning Parameters:  $5\text{ mV}$ ,  $9\text{ nA}$   
 (b)  $dI/dV$  spectra



(a) (b)  
 Figure 32  $dI/dV$  line spectra across the N dopant  
 (a) Size:  $5\text{ nm} \times 5\text{ nm}$ ; Scanning Parameters:  $10\text{ mV}$ ,  $9\text{ nA}$   
 (b)  $dI/dV$  line spectra recorded along the green arrow in (a)

The dopant clearly affects the shape of the  $dI/dV$  curve. Figures 31 and 32 both show significant increases in local density of states at around  $-300\text{ mV}$  for the dopant and areas immediately surrounding the dopant.

It should be mentioned that the tip status for Figures 31 and 32 is different from the tip status for Figure 30. The two different tip statuses produce different shapes of  $dI/dV$

spectra. However, the Dirac point located between -300 mV and -400 mV is detected by both tip statuses.

### 3.6 XPS Data

XPS data was used to verify the presence of N and its binding configurations. It has also helped identify concentrations of N and C. According to the results, the surveyed 1.0 ML graphene surface contained 96.0% C and 4.0% N. Therefore, the measured ratio of dopants to C was approximately 1:24.

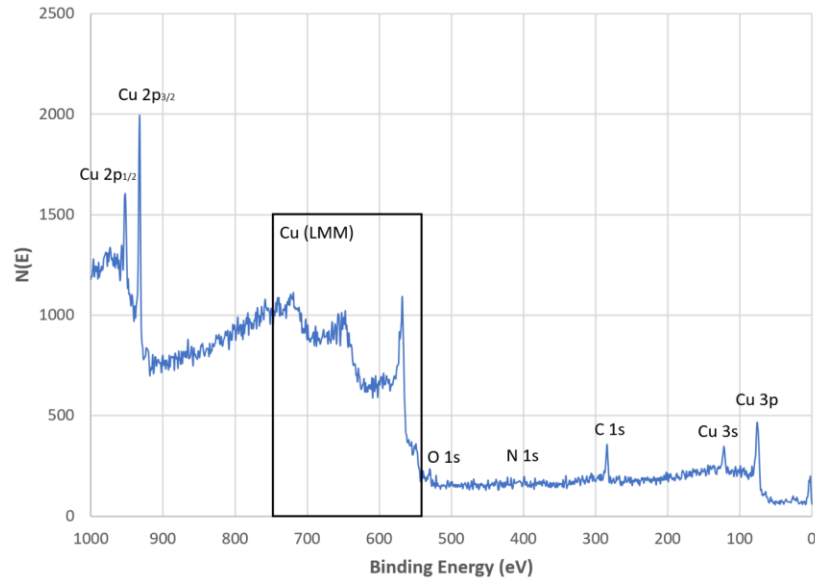


Figure 33 XPS survey scan

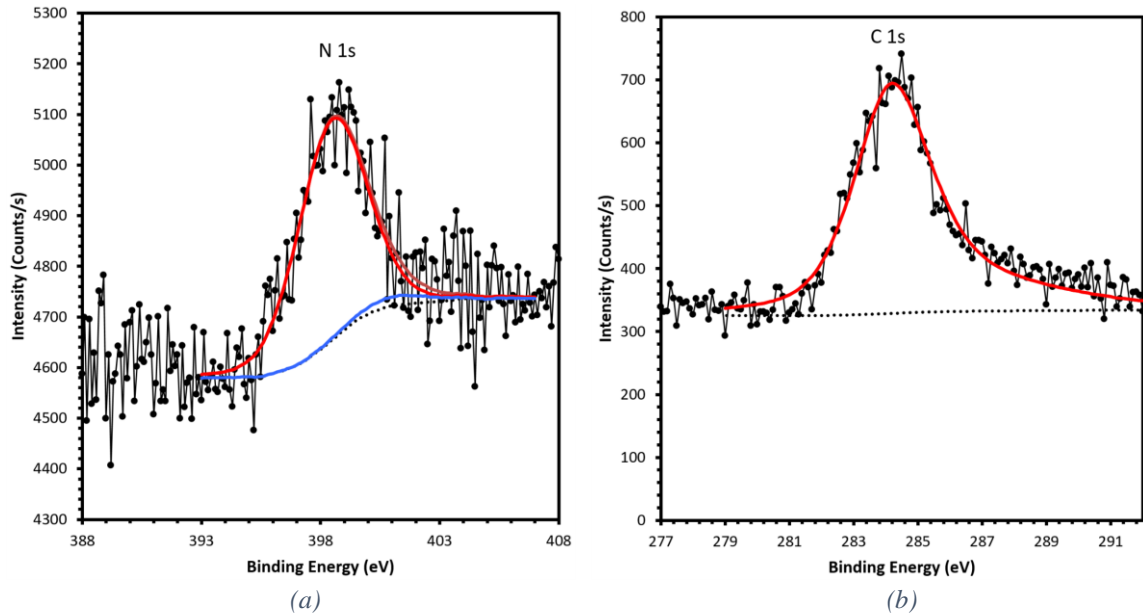


Figure 34 XPS spectra of (a) N 1s and (b) C 1s

The N 1s spectrum can be fitted with two peaks. The peak centered at 398.4 eV can be attributed to pyridinic N, and the peak centered at 401.2 eV can be attributed to graphitic N.<sup>37</sup> The pyridinic N accounts for 3.8% of the surface, and graphitic N accounts for the other 0.2%.

### 3.7 Discussion

It is possible that the observed rings of N dopants may not occur at higher annealing temperatures, which will be one of the focuses in future studies.

STM measurements show that the predominant doping configuration within graphene islands is graphitic N. XPS results indicate that, besides graphitic N, pyridinic N atoms also exist on the surface. One possible explanation is that the graphene edges are decorated with pyridinic N atoms, which is also in agreements with our speculation on the mechanism for the formation of dopant rings. The existence of pyridinic N and formation of dopant rings can potentially be understood by further STM measurements of graphene edges and density functional theory calculations.

The high ratio of pyridinic to graphitic N can be explained in two ways. First, it is possible that some pyridinic N is desorbed from the surface during annealing. This would lead to observed dopant rings with fewer graphitic N dopants than the pyridinic dopants which were originally on the edges. However, this explanation alone would require 19 times more pyridinic than graphitic N dopants, which is unlikely based on the STM results. A second factor must also contribute. Cycles of deposition and annealing introduce new islands of graphene which have edges with pyridinic N but no interior graphitic N rings. These two explanations together likely account for the measured difference between pyridinic and graphitic N.

## 4 Summary and Outlook

### 4.1 Summary

We have studied the synthesis of N-doped graphene on Cu(111) using the  $C_{59}NH$  molecule. For the first time, we discovered that N dopants in the graphene layer tend to form rings, which might be induced by the preferential binding of N at the graphene edges. XPS results have confirmed the existence of N dopants in the graphene layer. STM and XPS measurements suggest that graphitic N atoms exist within graphene islands and pyridinic N atoms exist on graphene edges.

### 4.2 Potential Applications

We expect N-doped graphene to be a common variation of graphene for industry. N-doped graphene may be used in computing, clean energy, fuel storage, supercapacitors, and more.

Tailoring the chemical and electrical properties in a graphene lattice is instrumental in finding the most efficient material for any given application. Using a single precursor molecule greatly simplifies the method by which this tuning can be achieved. Additionally, the ability to control dopant position relative to the graphene islands may be extremely useful. Graphene islands with tunable dopant rings could allow for unprecedented control over the properties shown in Table 1.

### 4.3 Questions for the Future

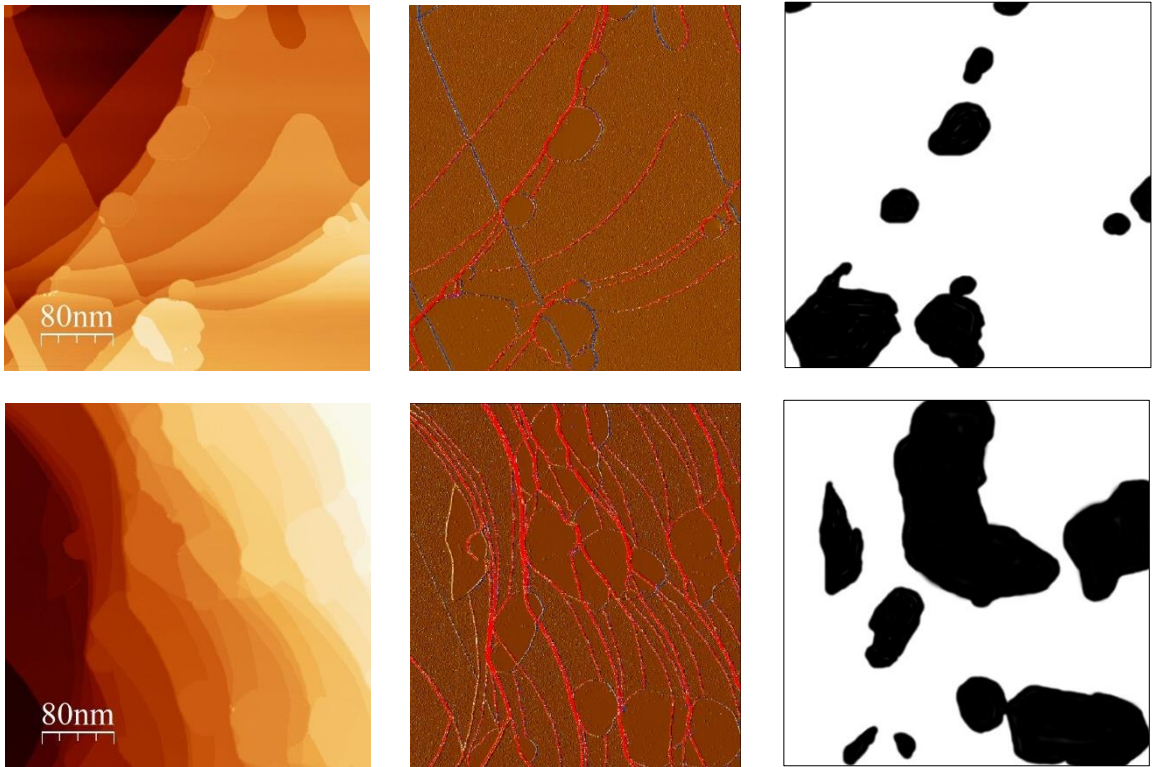
More precise measurements of the dopants' distributional stability should be conducted. It may be useful to anneal the sample at higher temperatures to determine whether or not the dopants remain in their positions with increased thermal energy.

Future research will be conducted to expand our understanding of the formation of dopant rings. We would like to determine whether graphene islands grow asymmetrically due to energy conditions or deposited molecule locations. To determine if the spacing between rings can be controlled, cycles of deposition and annealing will be conducted with variable deposition times or precursor dosage.

## Supplemental Information

### S.1 Calculating Graphene Coverages

To calculate the graphene coverages mentioned in Figures 25(a) and 26(a), the original topography (Z) images were processed using a height differential mode ( $dZ/dX$ ) which can help distinguish the graphene area from the bare Cu area. On the differentiated Z images, the graphene area is much smoother than the Cu area. The differentiated image was then opened with GIMP (GNU Image Manipulation Program), where the outlines of the graphene edges could be traced and filled in. The rest of the image was removed, as shown.



The black and white image was opened in MATLAB, where a simple code was used to count the total number of black pixels and divide it by the total number of pixels, outputting our ratios. The code was as follows:

```
X=im名称;  
X(X(:)<150)=1;  
X(X(:)>149)=0;  
a=sum(X(:));  
X(:)=1;  
b=sum(X(:));  
a/b
```

## S.2 Plotting Line Spectroscopy Data with Igor Pro

The two-dimensional plots in Figures 13(b), 30(b), and 32(b) were produced using raw data from the Nanonis software. The data was exported as multiple ASCII .dat files and concatenated into one .txt file in the Windows terminal. Because the file contains more information than is needed, the main .txt file was then opened with Microsoft Excel and unnecessary columns of data were removed.

The remaining columns are either Bias and Current or Bias and Lock-in Y (LIY is proportional to  $dI/dV$ ) depending on what we want to graph. These data sets represent two of our three axes for the eventual surface plot. The third axis representing position (relative to the first point along the line where data was taken) needed to be generated using information readily available in the .txt file. Excel VBA was used to create this information. An example of the code is below:

```
Sub jnposition(): Dim ws As Worksheet, N As String, R As Double, F As
    Range, frow As Long
    Set ws = ActiveSheet: N = "Experiment": frow = 1
    Do: Set F = ws.Range("B" & frow)
        R = Sqr((F.Offset(5, 0).Value - Cells(6, 2).Value) ^ 2 + (F.Offset(6,
            0).Value - Cells(7, 2).Value) ^ 2)
        F.Offset(17, 3).Value = "Position (m)"
        F.Offset(18, 3).Resize(256, 1).Value = R
        frow = frow + 274: Loop Until ws.Cells(frow, 2) = ""
    End Sub
```

The remaining unnecessary rows and columns were then removed. Though it was quite quick to get rid of the columns, the rows were a bit more difficult since there are so many files concatenated vertically into one long spreadsheet. Another subroutine was used:

```
Sub jndelrows()
    Columns("B:B").SpecialCells(xlCellTypeBlanks).EntireRow.Delete
End Sub
```

Occasionally, it may be preferable to use absolute values for a certain metric, as with Current in Figure 13(b). An additional subroutine can accomplish this:

```
Sub jnabsval()  
For Each Cell In Range("a1:a25700")  
If Cell.Value < 0 Then  
    Cell.Value = Abs(Cell.Value)  
End If  
Next Cell  
End Sub
```

The data can then be copied into a new .txt file, saved, and loaded into Igor Pro. Igor Pro interprets each column as a separate “wave” of data, but the “XYZ to Matrix” package allows us to create a matrix which can then be used to form the surface plot.

We chose the X-axis to be bias voltage, the Y-axis to be position, and the Z-axis to be current or  $dI/dV$ . The 2D plot was then generated using those specifications. The plot is scaled, labeled with units, and colored according to preference and clarity.

## References

- [1] Class for Physics. *Scientific Background on the Nobel Prize in Physics 2010: Graphene*. Royal Swedish Academy of Sciences, Stockholm, Sweden, 2010.
- [2] Castro Neto, A. H.; Guinea, F.; Peres, N. M. R.; Novoselov, K. S.; Geim, A. K. The Electronic Properties of Graphene. *Rev. Mod. Phys.* **2009**, *81*, 109.
- [3] Gao, L. Probing Electronic Properties of Graphene on the Atomic Scale by Scanning Tunneling Microscopy and Spectroscopy. *Graphene and 2D Materials* **2014**, *1*, 23-46.
- [4] Geim, A. K. Graphene: Status and Prospects. *Science* **2009**, *324*, 1530-1534.
- [5] Nair, R. R.; Blake, P.; Grigorenko, A. N.; Novoselov, K. S.; Booth, T. J.; Stauber, T.; Peres, N. M. R.; Geim, A. K. Fine Structure Constant Defines Visual Transparency of Graphene. *Science* **2008**, *320*, 1308.
- [6] Wang, X.; Sun, G. Z.; Routh, P.; Kim, D.-H.; Huang, W.; Chen, P. Heteroatom-Doped Graphene Materials: Syntheses, Properties and Applications. *Chem. Soc. Rev.* **2014**, *43*, 7067–7098.
- [7] Reddy, A. L. M.; Srivastava, A.; Gowda, S. R.; Gullapalli, H.; Dubey, M.; Ajayan, P. M. Synthesis of Nitrogen-Doped Graphene Films for Lithium Battery Application. *ACS Nano* **2010**, *4*, 6337-6342.
- [8] Novoselov, K. S.; Geim, A. K.; Morozov, S. V.; Jiang, D.; Zhang, Y.; Dubonos, S. V.; Grigorieva, I. V.; Firsov, A. A. Electric Field Effect in Atomically Thin Carbon Films. *Science* **2004**, *306*, 666–669.
- [9] Geim, A. K. Nobel Lecture: Random Walk to Graphene. *Rev. Mod. Phys.* **2011**, *83*, 851-862.
- [10] Kim, K. S.; Zhao, Y.; Jang, H.; Lee, S. Y.; Kim, J. M.; Kim, K. S.; Ahn, J.-H.; Kim, P.; Choi, J.-Y.; Hong, B. H. Large-Scale Pattern Growth of Graphene Films for Stretchable Transparent Electrodes. *Nature* **2009**, *457*, 706–710.
- [11] Kemp, K. C.; Seema, H.; Saleh, M.; Le, N. H.; Mahesh, K.; Chandra, V.; Kim, K. S.; Environmental Applications Using Graphene Composites: Water Remediation and Gas Adsorption. *Nanotechnology* **2013**, *24*, 235703.

- [12] Fei, X.; Zhang, X.; Lopez, V.; Lu, G.; Gao, H.-J.; Gao, L. Strongly Interacting C<sub>60</sub>/Ir(111) Interface: Transformation of C<sub>60</sub> into Graphene and Influence of Graphene Interlayer. *Journal of Physical Chemistry C* **2015**, *119*, 27550-27555.
- [13] Fei, X.; Neilson, J.; Li, Y.; Lopez, V.; Garrett, S. J.; Gan, L.; Gao, H.-J.; Gao, L. Controlled Synthesis of N-Doped Graphene on Ruthenium from Azafullerene. *Nano Letters* **2017**, *17*, 2887–2894.
- [14] Ito, Y.; Christodoulou, C.; Nardi, M. V.; Koch, N.; Sachdev, H.; Mullen, K. Chemical Vapor Deposition of N-Doped Graphene and Carbon Films: The Role of Precursors and Gas Phase. *ACS Nano* **2014**, *8*, 3337–3346.
- [15] Li, X.; Cai, W.; An, J.; Kim, S.; Nah, J.; Yang, D.; Piner, R.; Velamakanni, A.; Jung, I.; Tutuc, E.; Banerjee, S. K.; Colombo, L.; Ruoff, R. S. Large-Area Synthesis of High-Quality and Uniform Graphene Films on Copper Foils. *Science* **2009**, *324*, 1312-1314.
- [16] Binnig, G.; Rohrer, H. Scanning Tunneling Microscopy. *IBM Journal of Research and Development* **1986**, *30*, 355.
- [17] Binnig, G.; Rohrer, H. Nobel Lecture: Scanning Tunneling Microscopy – From Birth to Adolescence. *Rev. Mod. Phys.* **1987**, *59*, 615-625.
- [18] Fowler, R. H.; Nordheim, L. Electron Emission in Intense Electric Fields. *Proc. Roy. Soc. Lond. A* **1928**, *119*, 173.
- [19] Song, J. P.; Mørch, K. A.; Carneiro, K.; Thölén, A. R. STM Investigations of Solid Surfaces in Water and Air. *Surface Science* **1993**, *296*, 299-309.
- [20] Chen, C.J. *Introduction to Scanning Tunneling Microscopy*; Oxford University Press: New York, NY, 1993.
- [21] *Handbook of Chemistry and Physics*, 69<sup>th</sup> ed.; CRC Press: Boca Raton, FL, 1988.
- [22] *Operation manual for USM1500 SH*; Unisoku Co., Ltd.
- [23] Tsong, T. T. *Atom-Probe Field Ion Microscopy*; Cambridge University Press: Cambridge, United Kingdom, 1990.
- [24] Huang, D.; Liu, S.; Zeljkovic, I.; Mitchell, J. F.; Hoffman, J. E. Etching of Cr Tips for Scanning Tunneling Microscopy of Cleavable Oxides. *Review of Scientific Instruments* **2017**, *88*, 023705.

- [25] Ibe, J. P.; Bey Jr., P. P.; Brandow, S. L.; Brizzolara, R. A.; Burnham, N. A.; DiLella, D. P.; Lee, K. P.; Marrian, C. R. K.; Colton, R. J. On the Electrochemical Etching of Tips for Scanning Tunneling Microscopy. *Journal of Vacuum Science & Technology A: Vacuum, Surfaces, and Films* **1990**, *8*, 3570.
- [26] *K-cell Molecular Evaporator Manual*. Institute of Physics, Chinese Academy of Sciences.
- [27] Siegbahn, K. *Electron Spectroscopy for Atoms, Molecules, and Condensed Matter*. Inst. of Physics, Univ. Uppsala, Sweden, 1981.
- [28] Watts, J. F.; Wolstenholme, J. *An Introduction to Surface Analysis by XPS and AES*. Wiley: New York, NY, 2003.
- [29] Woodruff, D. P.; Delchar, T. A. *Modern Techniques of Surface Science*, 2nd ed.; Cambridge University Press: Cambridge, United Kingdom, 1994.
- [30] Wagner, C. D.; Muilenberg, G.E. *Handbook of X-Ray Photoelectron Spectroscopy*; Perkin-Elmer: Eden Prairie, MN, 1979.
- [31] Xin, N. N.; Huang, H.; Zhang, J. X.; Dai, Z. F.; Gan, L. B. Fullerene Doping: Preparation of Azafullerene C<sub>59</sub>NH and Oxafulleroids C<sub>59</sub>O<sub>3</sub> and C<sub>60</sub>O<sub>4</sub>. *Angew. Chem., Int. Ed.* **2012**, *51*, 6163–6166.
- [32] Bartles, L.; Meyer, G.; Rieder, K. -H. Controlled Vertical Manipulation of Single CO Molecules with the Scanning Tunneling Microscope: A Route to Chemical Contrast. *Applied Physics Letters* **1997**, *71*, 213-215.
- [33] Meyer, G.; Bartles, L.; Rieder, K. -H. Atom Manipulation with the Scanning Tunneling Microscope: Nanostructuring and Femtochemistry. *Superlattices and Microstructures* **1999**, *25*, 463-471.
- [34] Li, X.-F.; Lian, K.-Y.; Liu, L.; Wu, Y.; Qiu, Q.; Jiang, J.; Deng, M.; Luo, Y. Unraveling the Formation Mechanism of Graphitic N-Doping in Thermally Treated Graphene with Ammonia. *Scientific Reports* **2016**, *6*, 23495.
- [35] Zabet-Khosousi, A.; Zhao, L.; Pálová, L.; Hybersten, M. S.; Reichman, D. R.; Pasupathy, A. N.; Flynn, G. W. Segregation of Sublattice Domains in Nitrogen-Doped Graphene. *Journal of the American Chemical Society* **2014**, *136*, 1391-1397.

- [36] Zhao, L. Y.; He, R.; Rim, K. T.; Schiros, T.; Kim, K. S.; Zhou, H.; Gutierrez, C.; Chockalingam, S. P.; Arguello, C. J.; Pálová, L.; Nordlund, D.; Hybersetn, M. S.; Reichman, D. R.; Heinz, T. F.; Kim, P.; Pinczuk, A.; Flynn, G. W.; Pasupathy, A. N. Visualizing Individual Nitrogen Dopants in Monolayer Graphene. *Science* **2011**, 333, 999–1003.
- [37] Luo, Z.; Lim, S.; Tian, Z.; Shang, J.; Lai, L.; MacDonald, B.; Fu, C.; Shen, Z.; Yu, T.; Lin, J. Pyridinic N Doped Graphene: Synthesis, Electronic Structure, and Electrocatalytic Property. *Journal of Materials Chemistry* **2011**, 21, 8038-8044.